

# **Autism-linked Cullin3 germline haploinsufficiency impacts cytoskeletal dynamics and cortical neurogenesis through RhoA signaling**

Megha Amar<sup>1</sup>, Akula Bala Pramod<sup>1</sup>, Victor Munive Herrera<sup>1</sup>, Nam-Kyung Yu<sup>2</sup>, Lily R. Qiu<sup>3</sup>, Pan Zhang<sup>1</sup>, Patricia Moran-Losada<sup>1</sup>, Cleber A. Trujillo<sup>4,5</sup>, Jacob Ellegood<sup>3</sup>, Jorge Urresti<sup>1</sup>, Kevin Chau<sup>1</sup>, Jolene Diedrich<sup>2</sup>, Jiaye Chen<sup>1</sup>, Jessica Gutierrez<sup>1</sup>, Jonathan Sebat<sup>1,4,6</sup>, Dhakshin Ramanathan<sup>1</sup>, Jason P. Lerch<sup>3</sup>, John R. Yates III<sup>2</sup>, Alysson R. Muotri<sup>4,5,7,8\*</sup>, Lilia M. Iakoucheva<sup>1\*</sup>

<sup>1</sup> Department of Psychiatry, University of California San Diego, La Jolla, CA, USA

<sup>2</sup> Department of Molecular Medicine, The Scripps Research Institute, La Jolla, CA, USA

<sup>3</sup> Mouse Imaging Centre (MICe), Hospital for Sick Children, Toronto, ON, Canada

<sup>4</sup> Department of Cellular & Molecular Medicine, University of California San Diego, La Jolla, CA USA

<sup>5</sup> Department of Pediatrics/Rady Children's Hospital San Diego, University of California, San Diego, La Jolla, CA, USA

<sup>6</sup> University of California San Diego, Beyster Center for Psychiatric Genomics, La Jolla, CA, USA

<sup>7</sup> University of California San Diego, Kavli Institute for Brain and Mind, La Jolla, CA, USA

<sup>8</sup> Center for Academic Research and Training in Anthropogeny (CARTA), La Jolla, CA, USA

\*Corresponding authors: Lilia M. Iakoucheva ([lilyak@ucsd.edu](mailto:lilyak@ucsd.edu)) and Alysson R. Muotri ([muotri@ucsd.edu](mailto:muotri@ucsd.edu)).

# Summary

E3-ubiquitin ligase Cullin3 (*Cul3*) is a high confidence risk gene for Neurodevelopmental Disorders (NDD) including Autism Spectrum Disorder (ASD) and Developmental Delay (DD). We generated haploinsufficient *Cul3* mouse model to investigate brain anatomy, behavior, molecular, cellular, and circuit-level mechanisms dysregulated by *Cul3* mutations. Brain MRI of *Cul3* mutant animals found profound abnormalities in half of brain regions, including decreased volume of cortical regions and increased volume of subcortical regions. *Cul3* mutant mice exhibited social and cognitive deficits, and hyperactive behavior. Spatiotemporal transcriptomic and proteomic profiling of the brain implicated neurogenesis and cytoskeletal defects as key drivers of *Cul3* functional impact. Cortical neurons from mutant mice had reduced dendritic length and loss of filamentous actin puncta, along with reduced spontaneous network activity. Inhibition of small GTPase RhoA, a molecular substrate of Cul3 ligase, rescued dendrite length phenotype. This study identified RhoA signaling as a potential mechanism, through which *Cul3* mutation impacts early brain development.

# Introduction

Rare and *de novo* single nucleotide variants (SNVs) and copy number variants (CNVs) are major risk factors for neurodevelopmental disorders (NDDs). E3 ubiquitin ligase Cullin 3 (*Cul3*) is among genes most confidently implicated in NDDs with the genome-wide significant FDR<0.01 (Sanders et al., 2015). Exome sequencing studies have identified at least 20 mutations in the *Cul3* gene (13 protein-truncating mutations and 7 SNVs) in patients with Autism Spectrum Disorder (ASD), Developmental Delay (DD) and Schizophrenia (SCZ), with no *Cul3* mutations detected in healthy controls (**Figure 1A, Table S1**).

Cul3 belongs to a family of RING E3 ubiquitin ligases, and its molecular function has been well-characterized (Petroski and Deshaies, 2005). Cul3 regulates protein turnover by interacting with different adaptor proteins and ubiquitinating and directing for proteasomal degradation a variety of substrate proteins. As Cul3 can interact with multiple adapters, it is involved in regulation of a wide range of cellular processes including cytoskeleton organization, cell cycle regulation, protein trafficking, and stress response among many others (Petroski and Deshaies, 2005). Less is known about the function of Cul3 in neural cells, despite its increased expression during embryonic stages of brain development (Kang et al., 2011). Notably, homozygous deletion of *Cul3* in mice is lethal during early embryonic development (Singer et al., 1999).

One of the Cul3 adapters, KCTD13, has been implicated in mental disorders. KCTD13 is located within a large (~600 kb) CNV at 16p11.2 that confers high risk for psychiatric and developmental disorders (Malhotra and Sebat, 2012). We previously demonstrated that *Cul3* is co-expressed with *KCTD13*, and corresponding proteins physically interact during late mid-fetal period of brain development (Lin et al., 2015). This interaction is crucial for regulating the levels of a small GTPase RhoA, and *Cul3* knockdown leads to RhoA accumulation (Chen et al., 2009). RhoA is involved in neuronal migration, axon growth, dendrite formation, and cytoskeleton remodeling during brain development (Govek et al., 2011). Furthermore, upregulation of RhoA through its constitutive expression has been linked to suppression of dendritic spine morphogenesis and to dramatic loss of spines (Govek et al., 2011; Zhang and Macara, 2008). The contribution of RhoA to local regulation of axon growth has been recently demonstrated (Walker et al., 2012).

To investigate the impact of NDD-associated mutations on brain development, we generated *Cul3* haploinsufficient (*Cul3*<sup>+/-</sup>) mouse model using CRISPR/Cas9 genome engineering. We

introduced a germline 1bp insertion in exon 6 of *Cul3*, immediately adjacent to G754T (E246X) mutation detected in an ASD patient (O'Roak et al., 2012) (**Figure 1B**). Extensive characterization of the mutant *Cul3*<sup>+/-</sup> mice at multiple levels including brain neuroanatomy, behavior, transcriptomic and proteomic profiling of several brain region at three developmental time points, provided a detailed picture of the functional impact of *Cul3* mutation (**Figure 1C**). Our results demonstrate that *Cul3* haploinsufficiency severely impacts the developing brain and leads to social deficits and hyperactivity in mice. Dysregulation of genes and proteins involved in actin, intermediate filament and binding, pointed to cytoskeletal defects. Reduced synaptic connectivity and dendritic length were among most notable neuronal phenotypes observed in *Cul3*<sup>+/-</sup> mice. Importantly, upregulation of one of the *Cul3* substrates, small GTPase RhoA, a regulator of cytoskeleton, neuronal growth and migration, linked observed molecular defects with *Cul3* pathology. Treatment of cortical neurons with RhoA inhibitor Rhosin rescued dendritic length phenotype.

## Results

### *Cul3*<sup>+/-</sup> mice have severe brain anatomical defects

We introduced a 1bp frame-shifting insertion with CRISPR/Cas9 into exon-6 of *Cul3* one base pair upstream from the nucleotide mutated in an ASD patient (O'Roak et al., 2012) to generate *Cul3*<sup>+/-</sup> haploinsufficient mouse model on C57BL/6N background (**STAR Methods**). A heterozygous *Cul3*<sup>+/-</sup> founder mouse harboring the insertion was expanded via breeding with wild-type (WT) C57BL/6N mice for at least four generations to eliminate CRISPR off-target effects. In agreement with previous observations (Singer et al., 1999), homozygous *Cul3*<sup>-/-</sup> mutant animals were not viable. The heterozygous *Cul3*<sup>+/-</sup> mice were viable, reached a normal lifespan, and were fertile irrespective of sex. However, *Cul3*<sup>+/-</sup> mice had reduced body weight ( $P < 0.001$  for male and  $P < 0.01$  for female; t-test, **Figure 1D**). We validated the presence of mutation by Sanger sequencing (**Figure 1B**), and verified reduced levels of *Cul3* by qRT-PCR (**Figure 1E**) and Western blot (**Figure 1F**). These experiments demonstrated the reduction of *Cul3* expression in the brain of *Cul3*<sup>+/-</sup> mutant mice to approximately half of the level observed in WT littermates, thereby validating *Cul3* haploinsufficiency.

We analyzed the anatomy of fixed 8- to 10-week old adult (N=38) and postnatal day 7 (P7) (N=41) WT and *Cul3*<sup>+/-</sup> mouse brains using magnetic resonance imaging (MRI) (**Method Details**). We observed profound brain volume abnormalities in 46% (83/182, FDR<5%) of brain regions in *Cul3*<sup>+/-</sup> adult mice (**Figure 2A, Table S2**). Total brain volume, as well as relative grey matter volume, were both significantly lower in *Cul3*<sup>+/-</sup> mice compared to WT ( $P < 0.01$  and  $P < 0.05$ , respectively, two tailed t-test, **Figures 2B-2C**). No differences were observed in the white matter volume between *Cul3*<sup>+/-</sup> and WT mice (**Figure 2D**). With respect to specific brain regions, several areas of somatosensory cortex, entorhinal cortex and cerebellum were significantly decreased (**Figure 2E**), and midbrain, hypothalamus and thalamus were significantly increased in mutant mice (**Figure 2F**). Among other notable brain areas, many olfactory bulb regions, some of the hippocampal regions and primary visual cortex were also decreased (**Table S2**). Overall, the volume of many cortical regions was decreased, whereas the volume of many subcortical regions was increased in the adult mutant mice. Similar trends in brain volume changes were found in early postnatal brain, suggesting that the impact of *Cul3* mutation initiates during early brain development (**Figure S1, Table S2**).

Besides volume changes of specific brain regions, *Cul3*<sup>+/-</sup> mice displayed decreased cortical thickness, particularly within frontal cortical regions of the brain (**Figure 2G**). To investigate what layers contributed to the observed reduced thickness, we immunostained brain sections with mature neuron marker NeuN and upper layer neurons (II-IV) BRN2 (**Figure 2H**).

We observed reduction in neuron number from layers II-IV in the mutant suggesting that these layers are likely contributing to cortical thickness decrease

To assess whether programmed cell death, or apoptosis, may be responsible for reduced cortical thickness, we subjected nuclei of primary cortical neurons at DIV14 to terminal deoxynucleotidyl transferase dUTP nick end labeling (TUNEL). We observed significantly increased apoptosis in *Cul3*<sup>+/-</sup> mice compared to WT ( $P < 0.0001$ , t-test, **Figure 2I**). These results suggest that *Cul3* mutation severely impacts multiple brain regions in mice and affects cortical thickness, likely via increased apoptosis.

### ***Cul3* mutation causes behavioral deficits in mice**

Given profound changes of brain volume in *Cul3*<sup>+/-</sup> mice, we performed behavioral testing in adult animals to understand the impact of mutation on behavior. In the open field test, *Cul3*<sup>+/-</sup> mice travelled longer distances ( $P = 0.032$ ; t-test, **Figure 3A**) with higher speed ( $P = 0.032$ ; t-test; **Figure 3B**), suggesting hyperactivity. Data analysis in 10 min time bins revealed that they started to become more hyperactive after 20 min from the beginning of the test (**Figure 3C**). To assess whether hyperactivity is related to anxiety, we measured time spent in the center of the open field arena vs periphery, and observed no differences between *Cul3*<sup>+/-</sup> and WT (**Figure S2**). Self-grooming that may also suggest anxiety was not increased in the mutant mice (**Figure 3D**).

To investigate learning, short-term memory, and social interaction we first used novel object recognition test. In this task, *Cul3*<sup>+/-</sup> mice spent shorter time exploring novel object than WT mice ( $P < 0.05$ , t-test, **Figure 3E**). In the social interaction test, we first measured sniffing time of novel mouse vs novel object. *Cul3*<sup>+/-</sup> mice spent slightly less time sniffing the mouse than WT mice, and both *Cul3*<sup>+/-</sup> and WT mice preferred the mouse to the object (**Figure 3F**). However, when a novel mouse was introduced instead of the object, *Cul3*<sup>+/-</sup> mice spent the same time sniffing novel and familiar mouse, and this sniffing time was shorter compared to WT mice (**Figure 3G**). These results suggest that *Cul3*<sup>+/-</sup> mice are hyperactive and have impaired short-term memory and social interaction.

In addition to behavioral testing of adult mice, we investigated general developmental milestones in newborn mice through 21 days of age. There were no differences between genotypes in eye opening, ear-twitching, auditory startle, forelimbs grasping and other developmental milestones. The *Cul3*<sup>+/-</sup> mice demonstrated delayed performance in surface righting and cliff aversion tests, suggesting potential problems with motor control and vestibular difficulties (**Figure S3**). However, motor control deficiency did not persist into adulthood as demonstrated by higher distance traveled by the adult mutant mice in the open field test (**Figure 3A**).

### ***Cul3* mutation dysregulates cytoskeleton-related genes transcriptome-wide**

To understand how *Cul3* mutation impacts transcriptome during brain development, we performed RNA sequencing (RNA-seq) of 108 brain transcriptomes derived from three developmental periods (embryonic E17.5, early postnatal P7 and adult) and three brain regions (cortex CX, hippocampus HIP and cerebellum CB) of *Cul3*<sup>+/-</sup> mutant and WT mice (**Figure S4-S5**). Differential gene expression analyses was carried out to identify genes that were up- or down-regulated in the *Cul3*<sup>+/-</sup> mutant vs WT mice (**Method Details**). As expected, *Cul3* was the most differentially expressed gene in all datasets, validating haploinsufficiency. Dosage changes of *Cul3* gene also had transcriptome-wide *trans*-effect, dysregulating other genes. We identified hundreds of differentially expressed genes (DEG) between *Cul3*<sup>+/-</sup> mutant and WT mice at 10% FDR across developmental periods and brain regions (**Table S3**). In total, we identified 736, 1239



and 1350 unique DEGs in embryonic, early postnatal and adult periods, respectively. Likewise, in total we identified 727, 1641 and 1032 unique DEGs in CX, CB and HIP, respectively (**Figure S6**). Gene Ontology (GO) functional annotations of DEGs revealed enrichment of terms shared among multiple periods and regions that included cell adhesion, extracellular matrix organization, cell migration and motility, cell proliferation, and cilium- and microtubule-related functions (**Figure S7, Table S4**). Further analyses of DEGs that were contributing to the enriched GO terms identified clusters of genes that were up- or down-regulated in specific periods or regions (**Table S5**). GO annotation of these clusters highlighted terms shared by at least two clusters (**Figure 4A, Table S6**). Expression patterns of DEGs across periods selected from several shared GO terms highlight integrin and cilium for embryonic, cell adhesion and migration for early postnatal, and cytoskeletal processes for adult periods (**Figure 4B**).

To further investigate DEGs, we performed statistical enrichment of DEGs against curated gene lists with previous evidence for involvement in ASD (**Figures 4C-4D**). We observed enrichment of early postnatal and adult period DEGs in presynaptic and postsynaptic, highly intolerant to mutations ( $pLI > 0.99$ ), FMRP binding target, and high confident ASD risk genes, with the latter also enriched in the embryonic period (**Figure 4C**). With regards to the regions, CB was highly enriched in postsynaptic genes, and CX was enriched in ASD risk genes, synaptic, and highly intolerant to mutations genes (**Figure 4D**). This suggests that *Cul3* mutation dysregulates cytoskeletal genes, as well as genes relevant to ASD pathogenesis.

## **Proteomic profiling supports neuron cytoskeleton and neuron projection dysregulation**

Cul3 is a part of the ubiquitin-proteasome system that has significant role in protein turnover. To investigate the impact of Cul3 on regulation of protein expression, we carried out quantitative Tandem Mass Tag mass spectrometry (TMT-MS) on 48 brain samples derived from three developmental periods (embryonic E17.5, early postnatal P7 and adult) and two brain regions (cortex CX and cerebellum CB) of *Cul3*<sup>+/-</sup> mutant and WT mice (**Figure S8**). In most cases, tissues for proteomics experiments were dissected from the remaining brain hemisphere of the same samples that were used for the RNA-seq profiling.

Differential protein expression analyses identified hundreds to thousands of differentially expressed proteins (DEPs) across various datasets (**Table S7**). Overall, more DEPs were detected in embryonic brain than in early postnatal or adult, and more DEPs were detected in CX than in CB (**Figure S9**). For example, we identified 2,329 DEPs in embryonic, 986 in early postnatal and 402 in adult CX ( $FDR < 15\%$ ). GO annotations pointed to dysregulation of neuron-related and cytoskeletal functions (**Figure 5A**), with intermediate filament and neuron projection shared among different periods (**Table S8**). Interestingly, proteins significantly up- or down-regulated in *Cul3*<sup>+/-</sup> mutant were both contributing to neuron projection development GO function, whereas intermediate filament proteins were all upregulated in *Cul3*<sup>+/-</sup> embryonic CX (**Figure 5A**). Notably, three cytoskeletal proteins, neuronal intermediate filament protein (Ina), plastin (Pls3), and vimentin (Vim) were found to be upregulated in all proteomics datasets, supporting neuron cytoskeleton dysregulation by *Cul3* mutation with higher confidence (**Figure 5B**). We confirmed Pls3 upregulation by Western blot (**Figure 5C**). In addition, several other proteins with important neuronal and developmental functions were shared among datasets. They include receptor for netrin Dcc, required for axon guidance, contactin-associated protein-like Cntnap2, and treacle ribosome biogenesis factor Tcof1, involved in embryonic development of the craniofacial complex.

Similar to DEGs, we performed enrichment analyses of DEPs with genes previously implicated in brain development and ASD. Embryonic and early postnatal developmental periods demonstrated stronger enrichment of genes from essentially all tested datasets, including ASD

risk genes, compared to adult (**Figure 5D**). Likewise, cortex had stronger enrichments across all datasets than cerebellum (**Figure 5E**). This suggests that *Cul3* mutation impacts proteins expressed during early cortical development.

To further investigate the impact of *Cul3* on protein expression in mouse brain, we performed weighted protein co-expression network analysis (WPCNA) to identify modules of proteins with correlated expression that are impacted by the *Cul3* haploinsufficiency. We identified multiple protein co-expression modules in both, cortex and cerebellum. When modules were statistically tested for association with genotype, twenty one modules in CX (9 embryonic, 5 early postnatal and 7 adult) and eleven modules in CB (8 embryonic, 1 early postnatal and 2 adult) were detected as positively or negatively associated with *Cul3*<sup>+/-</sup> at 15% FDR (**Table S9**). GO annotations of the modules significantly associated with genotype (**Table S10-S11**) were in agreement with biological functions identified from DEG and DEP analyses. For example, *8pink* module was upregulated in *Cul3*<sup>+/-</sup> embryonic CX and enriched in intermediate filament proteins (Vim, Ina, Nes). Likewise, downregulated *2blue* module was enriched in neuronal and synaptic functions (neuron projection development, neuron differentiation, regulation of trans-synaptic signaling), with many genes previously implicated in ASD found within this module (CTNNB1, DPYSL2, NRXN1, STX1B, TBR1). Several modules contained proteins associated with chromatin and histone modification functions (*1turquoise* and *6red* in embryonic CX, and *6red* in early postnatal CX), and these modules were all upregulated in the *Cul3*<sup>+/-</sup> mouse. Further analyses of CX (**Figure 5F**) and CB (**Figure S10**) modules demonstrated significant enrichment of almost all modules in postsynaptic proteins, whereas downregulated modules with neuronal and synaptic functions (*2blue* in embryonic CX and *10purple* in early postnatal CX) were enriched in ASD risk genes. Several downregulated early postnatal CX modules with ion transport, neuron migration and neuron projection morphogenesis functions (*5green*, *10purple* and *11greenyellow*) were enriched in intolerant to mutations and constrained genes, as well as FMRP target genes (**Figure 5F**). Only one module from embryonic CX (*2blue*) was enriched in ASD risk genes from a largest ASD exome sequencing study (Satterstrom et al., 2020). Spatio-temporal brain proteome analyses further confirm dysregulation of neuronal and cytoskeletal proteins by *Cul3* mutation.

### ***Cul3*<sup>+/-</sup> cortical neurons have reduced dendritic growth and network activity**

The downregulated module *2blue* with neuronal and synaptic functions (**Figures 6A-6C**) was the only module that was significantly enriched in multiple categories of genes, including high-confident ASD risk genes (**Figure 5F**). Biological functions related to neuron projection development, neuron differentiation and trans-synaptic signaling with proteins known to be involved in dendrite and axon growth (EphA7, RAB family proteins, DPYSL2) were present in this module (**Table S10**). In addition, cytoskeletal proteins involved in regulation of actin polymerization from Arp2/3 and WASP complexes (ARPC2, ARPC3, EVL, BAIAP2) were found in this module. Notably, *2blue* module identified in embryonic CX was preserved across early postnatal and adult CX, and in embryonic CB, but not in early postnatal or adult CB (**Figure 6D**). Expression level of proteins from *2blue* module were decreased in *Cul3*<sup>+/-</sup> mice (**Figure 6E**).

To validate this module and to investigate potential neuronal defects in *Cul3*<sup>+/-</sup> mice, we examined neuron morphology and network activity of primary cortical neurons derived from mutant and WT animals. We calculated dendrite length and the number of neurites, along with soma size, of 14DIV neurons stained with MAP2 dendritic marker (**Figure 6F**). Tracing of MAP2-positive dendrites demonstrated reduction of total dendritic length and the number of neurites in *Cul3*<sup>+/-</sup> compared to WT mice (P=0.001; t-test; **Figures 6G-6H**). Soma size was not affected by the *Cul3* mutation (**Figure 6I**).

Altered neuron morphology could impact synaptic connectivity and alter neuronal network activity. We examined network activity using multielectrode array (MEA) recordings from 8 days old cortical neurons cultured *in vitro*. Representative raster plots of spontaneous spike activity from these cultures are shown in **Figure 6J**. Analyses of spontaneous neural recordings demonstrated significantly reduced weighted mean firing rate in *Cul3*<sup>+/-</sup> neurons compared to WT (P=0.002, t-test; **Figure 6K**). *Cul3*<sup>+/-</sup> neurons also had significantly reduced bursting activity (P = 0.007, t-test; **Figure 6L**). Quality controls included cell imaging to ensure comparable MEA plate coverage between genotypes, and total protein quantification from each well upon completion of the experiments.

### ***Cul3* dysregulates actin cytoskeleton and leads to loss of F-actin puncta in cortical neurons**

Proteomic profiling of mouse brain points to neuronal cytoskeleton as one of the cellular structures impacted by *Cul3* haploinsufficiency. Actin cytoskeleton plays an important role in neuronal growth, adhesion and migration. We found intermediate filament proteins to be upregulated across multiple DEP datasets (**Figure 5B**), along with upregulated embryonic CX module *8pink* containing these proteins (**Table S10**). At the same time, proteins involved in actin cytoskeleton-related processes (actin filament binding, actin cytoskeleton organization, regulation of actin cytoskeleton polymerization, regulation of actin filament length) were found to be downregulated in *Cul3*<sup>+/-</sup> brain. Specifically, we identified significantly downregulated *7black* module in the adult CX with actin cytoskeleton-related GO functions (**Figures 7A-7C**).

To validate potential actin cytoskeleton defects in *Cul3*<sup>+/-</sup> mouse, we co-stained 21 DIV *in vitro* cultured mature primary cortical neurons with Phalloidin-rhodamine and mature neuron marker MAP2 to quantify filamentous actin (F-actin) (**Figure 7D**). We observed significant reduction of Phalloidin intensity in *Cul3*<sup>+/-</sup> mutants (**Figure 7E**), as well as reduction of the number of F-actin puncta per dendrite length (**Figure 7F**). The loss of filamentous actin from spines (**Figure 7D, inset**) and dendrite shortening (**Figure 6G**) likely lead to defective cytoskeletal dynamics and changes in neural network activity observed in mutant mice (**Figures 6J-6L**).

### ***Cul3* haploinsufficiency leads to RhoA upregulation**

One of the direct molecular substrates of Cul3 ubiquitin ligase complex is a small GTPase RhoA. Cul3 ubiquitinates RhoA and directs it for proteasomal degradation. RhoA is an important regulator of actin cytoskeleton and neuron migration. We investigated RhoA levels in the developing brain by Western blot and observed significant RhoA upregulation in mutant embryonic and adult CX (**Figure 8A**). We also tested for levels of GTP-bound active form of RhoA (RhoA-GTP) and observed its significant increase in embryonic CX, in agreement with total RhoA upregulation (**Figure 8B**).

Since RhoA regulates neuronal actin cytoskeleton remodeling and neurite outgrowth, we investigated whether RhoA inhibition rescues previously observed dendritic length phenotype (**Figure 6G**). We took advantage of previously described pharmacological inhibitor of RhoA, Rhosin. Rhosin was shown to specifically block RhoA activation and induce neurite outgrowth (Shang et al., 2012). We repeated neuron morphometric analysis and used Rhosin (Rh) or vehicle (Vh) to treat primary cortical neuronal culture from 2 DIV until 14 DIV (**Figure 8C**). We replicated decreased dendritic length phenotype in Vh-treated *Cul3*<sup>+/-</sup> neurons, and Rhosin treatment rescued dendritic length defects in *Cul3*<sup>+/-</sup> to the level indistinguishable from the WT (**Figure 8D**). This suggests that RhoA upregulation in cortical neurons could be responsible for cellular, molecular and general neurodevelopmental defects observed in the *Cul3*<sup>+/-</sup> mutant mice.

## Discussion

Loss-of-function mutations in *Cul3* ubiquitin ligase are strongly associated with autism, developmental delay and schizophrenia. However, the molecular mechanism by which *Cul3* haploinsufficiency causes these diseases are unknown. Since *Cul3* is highly expressed in the embryonic human brain, and its expression decreases after birth, it is likely that its molecular impact is manifested during early brain development. In this study, we generated the first CRISPR/Cas9 mouse model carrying loss-of-function mutation in the same exon of *Cul3* gene as ASD patient's mutation. We characterized this model using brain MRI, transcriptomic and proteomic profiling, and provide evidence implicating cytoskeletal dynamics and cortical neurogenesis along with RhoA signaling as potential mechanisms of *Cul3* haploinsufficiency.

At the neuroanatomical level, we observed changes in about half of the imaged brain regions in adult *Cul3*<sup>+/-</sup> mutant mice suggesting profound impact of *Cul3* mutation on the brain. Many cortical structures (visual, somatosensory, entorhinal cortex, dentate gyrus and cerebellar cortex) were reduced, whereas subcortical structures (midbrain, hypothalamus and thalamus) were increased in the adult mutant mice. MRI imaging of early postnatal (P7) brain indicated that these changes initiate early in development, because similar albeit subtler alterations were observed in P7 brains. These changes in brain anatomy share similarities with other autism mouse models summarized in a previous study that clustered 26 autism mouse models into three groups by correlated size changes of distinct brain regions (Ellegood et al., 2015). *Cul3*<sup>+/-</sup> model is most similar to group three comprised of 16p11.2, *Mecp2*, and *CNTNAP2* models. Comparable brain structural changes were later reported in a different 16p11.2 deletion mouse model (Pucilowska et al., 2015), as well as in *TAOK2* mouse model (Richter et al., 2018). The similarities in brain anatomy could stem from dysregulation of the same molecular pathways that potentially involves RhoA signaling (Lin et al., 2015).

In addition to volumetric changes, we observed decreased cortical thickness and increased apoptosis of cortical neurons in the *Cul3*<sup>+/-</sup> brain. Neurons from upper layers are likely contributing to these phenotypes, given downregulation of proteins expressed in upper layer neurons (*Satb2*) and beta-tubulin marker protein (*Tubb3*) and upregulation of neuroprogenitor marker proteins (*Sox2* and *Nes*) in the embryonic cortex of *Cul3*<sup>+/-</sup> mutant mice. One possibility that could explain lower number of neurons in upper layers could be delayed neuronal maturation in addition to apoptosis. Another possibility is defective migration, which is also supported by our transcriptomic analyses.

Previously developed genetic autism mouse models (*SETD5*, *UBE3A*, *SHANK3*, Timothy syndrome) also observed reduced neurite outgrowth, sometimes in concert with reduced synaptic connectivity (Khatri et al., 2018; Krey et al., 2013; Moore et al., 2019; Yi et al., 2016). The iPSC-derived neurons from Timothy syndrome patients also exhibited dendrite retraction phenotype (Krey et al., 2013). Neuron morphology, and specifically dendrite length was reduced in *Cul3*<sup>+/-</sup> mice. Proteomic results identified module of co-expressed proteins with neuron projection development functions. Dendritic growth deficiencies in *Cul3*<sup>+/-</sup> neurons likely impacted synaptic connectivity and network activity, as we observed reduced firing rate and bursting activity in these neurons. RhoA is one of the proteins that controls neurite outgrowth, and RhoA upregulation was previously implicated in loss of spines and neurite retraction (Chen et al., 2009; Krey et al., 2013; Lin et al., 2015; Shang et al., 2012; Walker et al., 2012). Thus, reduced neurite outgrowth as a result of upregulated RhoA signaling could be a shared phenotype among different autism models.

In particular, the dysregulation of cytoskeletal proteins suggests a possible mechanism underlying cellular phenotypes observed in our *Cul3* haploinsufficiency model. Spatio-temporal



profiling of *Cul3* mouse brain converged on key biological processes involved in early brain development including extracellular matrix organization, cell adhesion, microtubule formation, neuron migration, motility and locomotion, and cilium-related functions. All these functions rely on structural cytoskeleton proteins, further emphasizing the importance of cytoskeletal integrity during neocortical development. It is likely that *Cul3* impacts a multitude of cytoskeletal proteins, including those involved in intermediate filament, microtubule and actin cytoskeleton organization, remodeling, binding and regulation. Cytoskeletal proteins were impacted to various degree in all developmental periods and regions, with three upregulated proteins (Vim, Pls3 and Ina) consistently shared by all datasets. Other proteins with actin-related functions formed a module downregulated in the mutant. We experimentally confirmed loss of filamentous actin puncta in *Cul3*<sup>-/-</sup> neurons, providing further evidence for cytoskeletal defects. Since F-actin is known to be abundant in spines of mature neurons, its loss suggests potential loss of spines. A recent study of a conditional *Cul3* mouse model reported reduced spines in prefrontal cortex-specific deletion of *Cul3* in agreement with our findings (Rapanelli et al., 2019). The same study implicated upregulation of Smyd3 histone methyltransferase in *Cul3* defects, however we did not detect this protein in our proteomics experiments. Another study reported protein translation defects, and specifically upregulation eIF4G1 protein, in another *Cul3* conditional model (Dong et al., 2019). We have detected eIF4G1 in all our proteomics datasets, however it was not significantly changed in mutants vs control (**Table S7**). Importantly, Vim and Pls3 were upregulated in one study (Rapanelli et al., 2019), and Pls3 was upregulated in another study (Dong et al., 2019) in agreement with our results.

We attribute observed cytoskeletal and neuronal defects to upregulation of RhoA signaling. First, we observed RhoA upregulation in embryonic and adult cortex of *Cul3* mutant mice. Second, we were able to rescue dendrite length phenotype by pharmacological inhibition of RhoA activity. Third, RhoA upregulation was found in other relevant ASD models, such as KCTD13 (Escamilla et al., 2017). KCTD13 is an adaptor for *Cul3* that regulate RhoA ubiquitination and degradation. Thus, downregulation of either KCTD13 or *Cul3* are expected to upregulate the levels of RhoA. A recent study of conditional *Cul3* model also observed RhoA upregulation in the cortex (Rapanelli et al., 2019). Most importantly, RhoA is a key regulator of actin cytoskeleton remodeling, neurite outgrowth, migration and spine formation during early cortical development (Azzarelli et al., 2014), and we observed defects in many of these pathways in *Cul3*<sup>-/-</sup> mouse. It is possible that *Cul3* dysregulates other pathways upstream or downstream of RhoA to cause these phenotypes. This possibility could not be ruled out by our study and needs further investigation.

## Acknowledgments

This work was supported by a grant to LMI and ARM from the National Institute of Mental Health (MH108528), and by grants to LMI and ARM (MH109885, Simons Foundation for Autism Research #345469), to LMI (MH105524, MH104766), to JRY and ARM (MH100175), and to JS (MH119746). RNA-seq data was generated at the UC San Diego IGM Genomics Center, University of California San Diego (grant P30CA023100). The images were acquired at the UCSD School of Medicine Microscopy Shared Facility (grant NS047101). We thank Barun Das for TUNEL data analysis, Punit Mehta for help with mouse behavior data analyses, Alessandra Porcu and Ben Romoli for histology support, Kaiyi Mu, Jasmine Le, and Camille Sotelo for help with image analysis.

## Author contributions

L.M.I. and A.R.M. conceived the study. M.A., A.B.P., V.M.H., N-K.Y., L.R.Q., P.Z., P.M-L., C.A.T., J.E., J.U., K.C., J.D., J.S., D.R., J.P.L., J.R.Y. III, A.R.M. and L.M.I. designed the experiments and analyses. M.A., V.M.H., N-K.Y., L.R.Q., C.A.T., J.U., J.D., and J.G. performed



experiments and analyses. A.B.P., P.Z., P.M-L., K.C., J.E., K.C., J.C., and D.R. performed computational data processing and analyses. M.A. and L.M.I. wrote the manuscript, with input from all co-authors. Supervision was performed by J.S., D.R., J.P.L., J.R.Y. III, A.R.M, and L.M.I.

## Materials and Methods

### Generation of *Cul3*<sup>+/-</sup> mice using CRISPR-Cas9 genome editing

For generating *Cul3* mouse model with the patient specific p.Glu246Stop (E246X) mutation (O’Roak et al. 2012), single-guide RNAs (sgRNA) and single stranded oligos (ssODN) were designed to create the E246X frameshift mutation. Two single guide (Sg) RNA Sg1- GGATTAATGAGGAAATAGAG Sg2- AGTAGAAGCTAGGATTAATG with little off-target specificity for *Cul3* (NM 016716.5) were designed using <http://crispr.mit.edu/> platform and CHOP-CHOP (<https://chopchop.cbu.uib.no/>). The specificity and efficiency of each sgRNA was validated using *in vitro* Cas9 cleavage assay. Generation of transgenic lines was performed by the UCSD Moores Cancer Center Transgenic Mouse Core Facility. Briefly, microinjections consisting of SgRNA1 (0.6μM of crRNA, 0.6μM tracrRNA), 0.5μM of ssODN and 30ng/μl Cas9 protein (PNA-Bio, USA) was injected in pronuclear stage embryos in the C57BL/6N genetic background. The exon-6 specific genotyping primers *Cul3*-ex6-Fwd: CTGCATGAAATGTGTCTTTAACTGT and *Cul3*-ex6-Rev: CCACCCCACTGCTAACTAGG were used for PCR genotyping followed by Sanger sequencing. The Heterozygous *Cul3* founder mouse harboring 1bp-insertion in exon6 was expanded via breeding with wild-type (WT) C57BL/6N mice. The carrier male *Cul3*<sup>+/-</sup> mice were bred for at least four generations before starting any experiments to eliminate off-target effect of CRISPR. *Cul3* heterozygous (*Cul3*<sup>+/-</sup>) mice were viable, reached normal lifespan, and were fertile irrespective of sex.

### Mouse behavioral testing

All experiments were approved by the Institutional Animal Care and Use Committees (IACUC) of the University of California San Diego. *Cul3*<sup>+/-</sup> and WT littermates were used for behavioral experiments. Male and female mice were group housed post-weaning, segregated by sex, with unrestricted access to food and water, and were kept on a 12 h light/12 h dark cycle. For all tests 1 hour of habituation to the room before each test was performed. *Cul3*<sup>+/-</sup> and their WT littermates were evaluated on the same day and by the same equipment. Testing for open field, social preference, object recognition, repetitive behavior and social behavior were conducted during the light phase (10 am-5 pm) on different days. All testing equipment was positioned inside a photo light box that have dim overhead fluorescent lighting (14 lux).

**Developmental milestones.** Development of reflexes and growth was evaluated as previously described (Hill et al., 2008). Reflexes were considered to be acquired only after they had been observed for 2 consecutive days.

**Open Field.** The apparatus measured approximately 43 x 43 x 33 cm (width x depth x height), the center was defined as the middle 26 x 26 cm. Mice were tested in a white open field for a total of 30 minutes per animal. The behavior and time spent in center vs borders was recorded for 30 minutes by video camera. The videos were analyzed by MATLAB software and scored for 10, 20 and 30 minutes.

**Novel object recognition.** On day 1 of the experiment, mice were familiarized with the training room (1 h) in their home cages. During the first day, the mice explored an empty chamber for 5 min (plastic chamber, 61x42x22 cm). On testing day, the animals were placed in the testing chamber for 1 min to re-habituate. Then two identical objects (plastic figures) were placed into the testing chamber. The mouse was placed in the chamber for 15 min to explore the objects. After a 3h delay, the mouse was placed in the testing chamber with one object identical to the

previous object, and a new object with different shape, texture and color. Over a 15-min time period, the relative amount of time the animal spends exploring the new object compared to the familiar one was quantified by MATLAB software.

**Repetitive behavior.** Each mouse was placed in a novel test cage with no bedding or food. The animal spent a total of 20 minutes in novel test cage (10 minutes for habituation, 10 minutes for observation). The last 10 minutes of repetitive behavior was scored for the following categories: self-grooming, circling, isolation, or another unusual behavior.

**Social preference test.** The three-chamber test was done in a social box and grids were purchased from Harvard Apparatus (Catalog #76-0673, #76-0674). The test was performed as previously described (Qin et al., 2018). One day before testing mice were habituated to the three-chamber apparatus, and were allowed to explore the apparatus for 10min, with empty grid at each side of the chamber. A plastic dish was placed on top of each grid to prevent climbing to the top. On test day, the test mouse was then placed in the center chamber and was free to explore the chambers for 10 min in each of the following phases: the first phase two identical non-social stimuli (Red lego blocks); the second phase non-social stimulus (yellow, gray and green Lego Blocks), and a social stimulus (age and sex matched mouse); the third phase familiar mouse and a novel mouse. The familiar mouse is the same mouse used in the second phase. The chamber was cleaned with 70% ethanol between phases. The chamber time and sniffing time was scored for the intervals of 10 min. Manual (blind analysis) and automated (MATLAB Software) methods of scoring chamber time and cylinder sniffing were used.

## **Magnetic Resonance Imaging (MRI) of adult and early postnatal (P7) mouse brain**

The cohort used for behavioral testing was subsequently used for adult brain MRI study.

**Perfusion.** Mice undergone behavioral testing (*Cul3<sup>+/-</sup>*: 10 male, 10 female; WT: 8 male, 10 female) were anesthetized with a ketamine/xylazine mix (10mg/kg) and intracardially perfused with 30mL of 0.1 M PBS containing 10 U/mL heparin (Sigma) and 2mM ProHance (a Gadolinium contrast agent), followed by 30 mL of 4% paraformaldehyde (PFA) containing 2mM ProHance. After perfusion, mice were decapitated and skin, lower jaw, ears and cartilaginous nose tip were removed as previously described (Nieman et al., 2018; Spencer Noakes et al., 2017). The brain within the skull was incubated in 4% PFA containing 2mM ProHance overnight at 4 degrees Celsius then transferred to 0.1M PBS containing 2mM ProHance and .02% sodium azide for at least 7 days prior to MRI scanning.

**Imaging.** After perfusion, a multichannel 7.0 Tesla MRI scanner (Agilent Inc., Palo Alto, CA) was used to image the brains within their skulls. Sixteen custom-built solenoid coils were used to image the brains in parallel. In order to detect volumetric changes via anatomical imaging, the following parameters were used: T2-weighted, 3-D fast spin-echo sequence, with a cylindrical acquisition of k-space, a TR of 350 ms and TEs of 12 ms per echo for 6 echoes, field-of-view equal to 20 × 20 × 25 mm<sup>3</sup> and matrix size equal to 504 × 504 × 630 mm<sup>3</sup>. These parameters output an image with 0.040-mm isotropic voxels. The total imaging time was 14 h.

**Analysis.** All images were registered through iterative linear and nonlinear registrations to create a consensus average brain image. Deformation fields were computed which describe the differences between each individual and the average. The Jacobian determinants of the deformation fields were then calculated as measures of volume at each voxel (Nieman et al., 2007). Structure volume was also calculated by warping a pre-existing classified MRI atlas onto the population atlas, which allowed for the calculation of 182 structures (Dorr et al., 2008; Steadman et al., 2014; Ullmann et al., 2013). Multiple comparisons were controlled for using the false discovery rate (FDR) (Genovese et al., 2002).

## Young mice (P7) - 56um DTI

**Perfusion.** For younger mice, a similar perfusion protocol was followed with minor modifications. 15ml instead of 30ml of perfusion solution was used at both stages of the intracardial perfusion. Additionally, the skin and other skull structures were not removed following decapitation to prevent possible damage to the skull and brain of the neonatal mouse.

**Imaging.** For younger brains, diffusion tensor imaging was used to optimize gray/white matter contrast, as brains have yet to undergo large scale myelination in development. The diffusion sequence is a 3D diffusion-weighted FSE, with TR= 270 ms, echo train length = 6, first TE = 30 ms, TE = 10 ms for the remaining 5 echoes, one average, FOV = 25 mm x 14 mm x 14 mm, and a matrix size of 450 x 250 x 250, which yielded an image with 56  $\mu$ m isotropic voxels. One b=0 s/mm<sup>2</sup> image is acquired and 6 high b-value (b = 2147 s/mm<sup>2</sup>) images were acquired at the following directions (1,1,0), (1,0,1), (0,1,1), (-1,1,0), (-1,0,1) and (0,1,-1) corresponding to (G x ,G y ,G z ). Total imaging time was ~ 14 hours.

**Analysis.** First, the six high b-value images were averaged together to make a high contrast image necessary for accurate image registration. Then, all average high b-value images were linearly and nonlinearly registered together to create a consensus average brain. Deformation fields, which describe the deformations needed to take each individual mouse anatomy into the consensus average space, were calculated, and the Jacobian determinant of those deformation fields were then calculated as measures of volume at each voxel. Structure volume was also calculated by warping a pre-existing classified MRI atlas onto the population atlas, which allowed for the calculation of 56 structures. Multiple comparisons were controlled for using the false discovery rate (FDR) (Genovese et al., 2002).

To calculate the change in region-specific volumes for a larger regions such as somatosensory cortex, cerebellum and entorhinal cortex (**Figure 2E**), the sum of the volumes of all sub-regions comprising each of these larger regions was calculated for each animal. Then, the mean, standard deviation, effect size and % difference were calculated for WT and *Cul3*<sup>+/-</sup> groups. The two tailed T-test was used for comparing the statistical differences.

## Immunohistochemistry

Mice were deeply anesthetized by xylazine and ketamine and were perfused with 4% paraformaldehyde (PFA). Whole brain tissues were extracted and dehydrated in a 30% sucrose solution at 4°C overnight. The 30  $\mu$ m thick brain slices were prepared using a cryostat (Leica, Germany). Slices were rinsed in 0.01 M PBS, permeabilized with 0.1% TritonX-100 in PBS and blocked in 3% FBS (with 0.1% Triton X-100) for 1 h. Primary antibody against NeuN (mouse 1:1000, Millipore, USA), BRN2 (rabbit 1:1000, cell signaling technology, USA) was added for overnight incubation at 4°C. Donkey anti-rabbit Alexa 555 and anti-mouse Alexa 488 secondary antibody (Life Technology, Camarillo, CA, USA) was added at room temperature for 2 h incubation. After PBS rinsing, DAPI was added for nuclear staining. Fluorescent images were taken on Leica SP8 confocal microscope using 10x inverted objective and quantification was done using ImageJ (NIH).

## Western Blotting

The small fraction of tissue lysates prepared for mass-spectrometry experiments were used for Western Blotting. The 10-15ug of total protein from WT and *Cul3*<sup>+/-</sup> cerebral cortex, cerebellum or hippocampus were resolved by SDS-PAGE and transferred onto PVDF Immobilon-P membranes (Millipore). After blocking with 5% nonfat dry milk in 1X TBS with 0.1% Tween-20 (TBST) for 1h at room temperature, membranes were first probed overnight with the appropriate primary antibodies in 3% BSA in TBST, and then after 1h of incubation with corresponding host

specific HRP-conjugated secondary antibody (Abcam). Membranes were developed using the EZ-ECL chemiluminescence detection kit (Denville Scientific). The following primary antibodies were used: anti-Cul3 (1:1000; Cell Signaling), anti-RhoA (1:1000; Cell Signaling), and anti-Gapdh (1:5000; Sigma Aldrich) as a loading control. Quantification was performed by densitometry with ImageJ software.

### **Primary cortical neuron culture**

Cortices were dissected from WT and *Cul3*<sup>-/-</sup> mouse embryonic brains at E17.5. Cortex from each brain was cultured individually. Dissociation was initiated by incubating the dissected cortices in 1ml of Accumax (Innovative Cell Technologies Inc) for 30 min at 37degree followed by 5min incubation in 10 mg/ml DNaseI (Sigma Aldrich), the dissociated cells were gently triturated with fire-polished glass pasteur pipette to make single cell suspension, and then passed through 40-micron nylon filter to remove any non-dissociated tissue. Cells were counted with cell counter (BioRad) and 1x10<sup>5</sup> cells were seeded onto glass coverslip coated with 0.01 % P-L-ornithine and 5ug/mL mouse natural laminin in 24-well plates. The plating media contained Neurobasal medium, 2% B27 supplement, 10% horse serum, 1% penicillin/streptomycin, and 2 mM L-glutamine (Invitrogen). After 12 hr, media was changed to serum-free feeding media containing Neurobasal medium, 2% B27 supplement, 1% penicillin/streptomycin, and 2 mM L-glutamine. At DIV2-4, cultures were treated with 1mM Cytosine b-D-arabinofuranoside hydrochloride (Ara-C) (Sigma Aldrich) to inhibit glial cell proliferation. Cultures were maintained at 37 degree, 5% CO<sub>2</sub>. All media components were from GIBCO unless otherwise specified.

### **Immunocytochemistry**

Coverslips containing primary cortical neurons were fixed in 4% paraformaldehyde (PFA) for 15 min and washed three times with PBS. Permeabilization and blocking was performed with 3% Bovine Serum Albumin (BSA, Sigma-Aldrich), 0.1% Triton X-100 (Sigma Aldrich) in PBS for one hour at room temperature. The coverslips were then incubated overnight at 4°C with primary antibodies diluted in solution containing 3% BSA. PBS was used to wash the primary antibodies and the coverslips were incubated with secondary antibodies in solution containing 3% BSA for 1.5 h at room temperature. The following primary antibodies were used for immunostaining: MAP2 (rabbit 1:1000, cell signaling technology); Rhodamine Phalloidin (Cytoskeleton). Alexa Fluor Dyes (Abcam) were used at 1:1000 dilution as secondary antibodies. Nuclei were visualized with DAPI (1:25000, Life Technologies). Slides were mounted using ProLong Gold antifade reagent (Invitrogen) and analyzed under a fluorescence microscope (Leica SP8). Image analysis was performed with ImageJ software

### **Morphological Analysis**

Images were taken with Leica SP8 confocal microscope with oil-inverted 40x objective and processed and analyzed with ImageJ 1.5 software. For soma area calculation, the perimeter of the MAP2+ cell body was manually outlined and measured. For total dendrite length analysis, the simple neurite tracer plugin for ImageJ 1.5 was used. Map2 positive neurites from each neuron were traced and the dendrite length was calculated by adding individual lengths for every neuron. F-actin positive puncta on dendrites was calculated by visually counting all protrusions from a dendrite within a 15–25 mm distance starting at a secondary branch point. One to three dendritic segments were analyzed per neuron. The no of f-actin puncta was normalized by dendritic length, similar region were also used for quantification of F-actin intensity using Image J 1.5.

### **Pharmacological treatment of cortical neurons**



For phenotype rescue experiments, cultured cortical neurons were grown in Rhosin-treated neurobasal media. Rhosin (Tocris) was added to the final concentration of 10 $\mu$ m to the media during at 2 DIV stage. The same amount of Rhosin was added after every 4 days during all subsequent media changes. The cells were grown for 14 days, at which dendrite staining was carried out. An equivalent amount of vehicle (Dimethylsulfoxide, DMSO) was added to a final concentration of 0.001% to growth media to obtain vehicle-treated WT and *Cul3*<sup>-/-</sup> cortical neurons.

## **TUNEL Assay**

We used a terminal deoxynucleotidyl transferase (TdT) dUTP nick-end labeling (TUNEL) assay to measure the apoptosis of the primary cortical neurons and precursor cells. The assay was performed using APO-BrdU TUNEL assay kit (Invitrogen) as described by manufacturer. In brief, primary cortical neurons were fixed with 4%PFA followed by O/N incubation in 70% ethanol at -20degree followed by PBS washing. A freshly prepared TUNEL reaction buffer (50  $\mu$ L per sample) was added at 37°C incubation for 1 h. After rinsing with the rinse buffer, the Propidium Iodide(PI) was used for nuclei staining. The cells were counted by FACS, only dual positive cells i.e. PI AND BrdU-488 positive cells were used for analysis.

## **Multi-electrode array (MEA) recording**

Primary cortical neurons from WT and *Cul3*<sup>-/-</sup> E17.5 embryos were cultured on 12-well Axion Maestro multielectrode array (MEA) plates (Axion Biosystems, Atlanta, GA, USA). Each 12-well MEA plate from Axion Biosystems was coated with 100  $\mu$ g/mL poly-L-ornithine and 10  $\mu$ g/mL laminin for 24 h before seeding. 1.5x10<sup>6</sup> neurons were plated on the coated MEA plates and a half-medium change was performed every other day using neurobasal+B27 feeding medium. Spontaneous spike activity was recorded on 8 DIV. Recordings were performed at 37 °C using a Maestro MEA system and AxIS Software Spontaneous Neural Configuration (Axion Biosystems). Briefly, Spikes were detected with AxIS software using an adaptive threshold and then analyzed using Axion Biosystems' Neural Metrics Tool. Spike time stamps were exported to Neuroexplorer (Axion Biosystems) for the creation of raster plots. Bright-field images were captured to assess for cell density and electrode coverage.

## **RNA isolation for RNA-Seq and qPCR**

Total RNA was extracted at three developmental time periods (embryonic E17.5, early postnatal (day 7) and adult (4-6weeks)) from three brain regions (cerebral cortex, hippocampus, and cerebellum) of WT and *Cul3*<sup>-/-</sup> mice using the QIAGEN RNAeasy isolation kit (QIAGEN) following manufacturer's instructions. RNA sequencing was performed using equal input amount of total RNA for each sample. RNA samples were ribodepleted using Ribo-Zero rRNA Removal Kit (Illumina) and library preparation was performed using the True-Seq Stranded Total RNA kit for Illumina Sequencing according to the manufacturer's instructions. Paired-end RNA sequencing (2x150bp) was performed on an Illumina HiSeq4000 to an average depth of 40M reads per sample.

For Quantitative RT-PCR (qPCR) experiments (**Figure 1E**), cDNA was synthesized starting from 100ng of total RNA with the SuperScript III First-Strand Synthesis kit and oligo dT (Invitrogen). The qPCR was performed using the CFX96 Touch™ Real-Time PCR Detection System (Bio Rad) using Power SYBR Green PCR Master Mix (Applied Biosystems). GAPDH and  $\beta$ -actin were used as housekeeping genes for normalization. Fold change in expression was calculated using the  $\Delta\Delta C_t$  method. Data represented as levels of *Cul3* normalized to GAPDH levels.

## **RNA-sequencing Data Processing Pipeline**



All 108 FASTQ files (36 embryonic, 36 early postnatal and 36 adult) (**Figure S4**) were run through a unified paired end RNA-Seq processing pipeline. Pipeline source code can be found on <https://github.com/lakouchevaLab/CUL3>. All fastqs were trimmed for adapter sequence and low base call quality (Phred score < 30 at ends) using Cutadapt (v1.14). Trimmed reads were then aligned to the GRCm38.p5 (mm10) reference genome via STAR (2.5.3a) using comprehensive gene annotations from mouse Gencode (v16). Gene-level quantifications were calculated using RSEM (v1.3). Quality control metrics were calculated using RNA-SeQC (v1.1.8), featureCounts (v1.6.), PicardTools (v2.12), and Samtools (v1.3) (**Table S12, Figure S5**).

## **RNA-Seq Quality Control, Normalization and Differential Gene Expression Analysis**

RNA-Seq Quality Control and Normalization Expected counts were compiled from gene-level RSEM quantifications and imported into R for downstream analyses. Expressed genes were defined as genes with TPM > 0.1 in at least 80% of samples from each genotype (WT and *Cul3*<sup>+/−</sup>). A total of 17,363; 18,656; and 18,341 expressed genes from embryonic cortex, cerebellum, and hippocampus, respectively; 18,921; 18,276; and 18,396 expressed genes from early postnatal cortex, cerebellum, and hippocampus, respectively; and 18,061; 17,835; and 17,654 expressed genes from adult cortex, cerebellum, and hippocampus, respectively, were used in the downstream analysis using the mouse Gencode (v16) annotation gtf file. Only expressed genes were included into the analysis.

To account for possible batch effects, batch effect removal was performed using EDASeq R package (Risso et al., 2011) and “remove unwanted variation” (RUVs) package in RUVseq (Risso et al., 2014). Initial normalization of count data was done using upper quartile normalization (Risso et al., 2011), followed by RUVseq. The parameter k in RUVseq was set to the minimum value that separated the samples based on genotypes on the PCA plot (maximum k=10). RUVs with different k values ranging from 3 to 8 were used after defining groups based on genotype (i.e. WT vs *Cul3*<sup>+/−</sup>). Differential gene expression analysis was performed with edgeR (Robinson et al., 2010) using the negative binomial GLM approach and by considering design matrix that includes both covariates of interest (Genotype and Gender) and the factors of unwanted variation. Genes with a false discovery rate (FDR ≤ 0.1, Benjamini-Hochberg multiple testing correction) were considered significant and used for further downstream processing and analysis.

Fisher p-value combination with metaRNASeq R package (Rau et al., 2014) was used to detect differentially expressed genes in period- and region-wise datasets. Genes with FDR ≤ 0.1 derived from p-value combination were hieratically clustered, and GO terms were obtained from 21 clusters using gProfiler (Reimand et al., 2007) (**Table S5-S6**). GO terms were subsequently hieratically clustered using log fold GO enrichment for **Figure 4B**.

## **Gene Ontology enrichment analysis**

Enrichment for Gene Ontology (GO; biological process and molecular function) was performed using gProfiler R package (Reimand et al., 2007). Background was restricted to the expressed set of genes by period (embryonic, early postnatal, adult) or region (cortex, cerebellum and hippocampus) whenever appropriate. Ordered query was used, ranking genes by FDR-corrected p-value.

## Enrichment analysis of gene sets

Enrichment analyses were performed using several established, hypothesis-driven gene sets including syndromic and highly ranked (1 and 2) genes from SFARI Gene database (<https://gene.sfari.org/database/gene-scoring/>); pre- and post-synaptic genes from SynptomeDB (Pirooznia et al., 2012); genes with loss-of-function intolerance (pLI) > 0.99 as reported by the Exome Aggregation Consortium (Karczewski et al., 2017); highly constrained genes (Samocha et al., 2014); and FMRP targets (Darnell et al., 2011). Fisher-exact test was used to calculate the enrichment of significantly differentially expressed genes for each curated gene set. The background lists were the union of all analyzed genes. Significance values of the results were corrected for multiple hypothesis testing using Benjamini-Hochberg corrections.

## Quantitative TMT-Mass Spectrometry

**Sample preparation.** TMT mass-spectrometry experiments were performed on the WT and *Cul3*<sup>-/-</sup> cerebral cortex and cerebellum at three developmental periods (embryonic, early postnatal and adult). Tissues were collected from the remaining half of hemisphere of the brains used for RNA-seq experiments (except for embryonic and adult cerebellum), and snap-frozen in liquid nitrogen. The tissue was lysed in RIPA buffer (20 mM Tris, pH 7.4, 150 mM NaCl, 1 mM EDTA, 1% sodium deoxycholate and 1% Triton X-100) supplemented with 1xEDTA-free complete protease inhibitor mixture (Roche) and phosphatase inhibitor cocktails-I, II (Sigma Aldrich). The lysates were centrifuged at 16,000xg at 4°C for 30min, and the supernatants were collected. Protein concentration was quantified by modified Lowry assay (DC protein assay; Bio- Rad). Lysates were subjected to methanol-chloroform precipitation, resuspended in 8M urea in 50 mM TEAB, reduced (10 mM TCEP at room temperature for 25 min) and alkylated (50 mM chloroacetamide at room temperature in the dark for 20 min). After another round of methanol-chloroform precipitation, pellets were dissolved by adding 6M urea in 50 mM TEAB, and the protein concentration was estimated by BCA assay (Thermo, 23225). LysC/Tryp (Promega, V5073) was added by 1:25 (w/w) ratio to the proteins. After 3-4 h of incubation with 850 rpm shaking at 37°C, reaction mixture was diluted with 50 mM TEAB for urea to be less than 1 M. After the o/n digestion, peptide concentration was estimated by colorimetric peptide BCA assay (Thermo, 23275), and the peptides were labelled with TMT 10-plex reagents (Thermo, 90110) for one hour, followed by 15 min quenching with hydroxylamine according to the manufacturer's protocol. Equal amounts of reaction mixtures for each channel were pooled together and dried using SpeedVac. Dried peptides were resuspended in 0.1% TFA and fractionated using Pierce™ High pH reversed-phase peptide fractionation kit (Thermo, 84868) and then dried in SpeedVac.

**Mass spectrometry.** Each fraction was dissolved in buffer A (5% acetonitrile, 0.1% formic acid) and injected directly onto a 25 cm, 100µm-ID column packed with BEH 1.7µm C18 resin (Waters). Samples were separated at a flow rate of 300 nL/min on nLC1000 (Thermo). A gradient of 1–30% B (80% acetonitrile, 0.1% formic acid) over 160 min, an increase to 90% B over another 60 min and held at 90% B for a final 20min of washing was used for 240 min total run time. Column was re-equilibrated with 10µL of buffer A prior to the injection of sample. Peptides were eluted directly from the tip of the column and nanosprayed directly into the mass spectrometer Orbitrap Fusion by application of 2.8 kV voltage at the back of the column. Fusion was operated in a data dependent mode. Full MS1 scans were collected in the Orbitrap at 120K resolution. The cycle time was set to 3s, and within this 3s the most abundant ions per scan were selected for CID MS/MS in the ion trap. MS3 analysis with multi-notch isolation (SPS3) (McAlister et al., 2014) was utilized for detection of TMT reporter ions at 60K resolution. Monoisotopic precursor selection was enabled, and dynamic exclusion was used with exclusion duration of 10s.

**Protein identification and quantification.** Tandem mass spectra were extracted from the .raw files using Raw Converter (He et al., 2015) with monoisotopic peak selection. The spectral files from all fractions were uploaded into one experiment on Integrated Proteomics Applications (IP2, Ver.6.0.5) pipeline. Proteins and peptides were searched using ProLuCID (Xu et al., 2015) and DTASelect 2.0 (Tabb et al., 2002) on IP2 against the UniProt reviewed Mus musculus protein database with reversed decoy sequences (UniProt\_mouse\_reviewed\_contaminant\_05-25-2018\_reversed.fasta from IP2 standard database). Precursor mass tolerance was set to 50.0 ppm, and the search space allowed both full- and half-tryptic peptide candidates without limit to internal missed cleavage and with a fixed modification of 57.02146 on cysteine and 229.1629 on N-terminus and lysine. Peptide candidates were filtered using DTASelect parameters of -p 2 (proteins with at least two peptides are identified) -y 1 (partial tryptic end is allowed) --pfp 0.01 (protein FDR < 1%) -DM 5 (highest precursor mass error 5 ppm) -U (unique peptide only). Quantification was performed by Census(Park et al., 2008) on IP2.

### **Differential protein expression analysis**

Proteomics data was first summarized to peptide level by adding up the intensities of constituting spectra. Quantitation results from different TMT runs were merged and normalized using the pooled samples channel which was present in all runs. For each peptide, multiple measurements from the same subject were collapsed to one measurement by taking the sum of all measurements. Batch effects from the summarized protein-level data for each dataset were removed using ComBat (Johnson et al., 2007). The data was then  $\log_2$  transformed. Differentially expressed proteins were identified using function lmFit in limma (Ritchie et al., 2015) followed by eBayes moderation of standard errors (Phipson et al., 2016). Resulting P-values were FDR-corrected using the Benjamini-Hochberg method to control for multiple comparisons.

### **Weighted protein co-expression network analysis**

We used Weighted Gene Co-expression Network Analysis (WGCNA) (Zhang and Horvath, 2005) to define modules of co-expressed proteins from proteomics data. Proteomics data was first summarized to protein level by adding up the channel intensities of constituting peptides for each of six datasets derived from two brain regions (cortex and cerebellum) and three developmental periods (embryonic, early postnatal and adult). Batch effects from the summarized protein-level data for each dataset were removed using ComBat (Johnson et al., 2007), followed by  $\log_2$  transformation. Modules were estimated using the blockwiseModules function with the following parameters: corType=bicorr; networkType=signed; pamRespectsDendro=F; mergeCutHeight=0.1. Some parameters were specific to each dataset. For embryonic cortex: power=18; deepSplit=0; minModuleSize=100; for early postnatal cortex: power=18; deepSplit=0; minModuleSize=100; for adult cortex: power=18; deepSplit=0; minModuleSize=20; for embryonic cerebellum: power=22; deepSplit=0; minModuleSize=40; for early postnatal cerebellum: power=26; deepSplit=0; minModuleSize=150; and for adult cortex: power=12; deepSplit=2; minModuleSize=40. Module eigengene-genotype associations were calculated using linear regression model. Significance p-values were FDR-corrected to account for multiple comparisons. Genes within each module were prioritized based on their module membership (kME), defined as correlation to the module eigengene. Module preservation (**Figure 6D**) was tested using the “Module Preservation” function from WGCNA.

### **Quantification and statistical analysis**

The statistical analyses for above experiments were performed using Prism software (GraphPad). Statistical tests used and exact values of n are described in Figure legends. Significance was

defined as  $p < 0.05$  (\*),  $p < 0.01$  (\*\*), or  $p < 0.001$  (\*\*\*). Blinded measurements were performed for any comparison between control and *Cul3*<sup>+/-</sup> genotypes.

## Main Figures titles and legends

**Figure 1. Generation and characterization of *Cul3*<sup>+/-</sup> mouse model.** (A) Loss-of-function and missense mutations in *Cul3* gene identified in the patients with neurodevelopmental disorders. ASD, autism spectrum disorder; SCZ – schizophrenia; DD – developmental delay. The location of E246X patient's mutation from this study is highlighted in violet box. (B) Schematic representation of mouse line generation using CRISPR/Cas9 genome editing. cDNA sequence trace showing 1-bp insertion (purple) in exon 6 is shown. Single guide (Sg) RNA is shown in blue, PAM site is shown in red. Sanger sequencing diagram is shown at the bottom. (C) Overview of the study design and analyses. (D) (left panel) Representative image of adult (8-weeks old) WT and *Cul3*<sup>+/-</sup> males demonstrating smaller body size of *Cul3*<sup>+/-</sup> mutants. (Right panel) Both adult male and female *Cul3*<sup>+/-</sup> mice have reduced body weight as compared to their WT littermates (\*\*\* $p < 0.001$ ; \*\* $p < 0.01$ ; Two-tailed T-test) (WT  $n = 11$  male/12 female; *Cul3*<sup>+/-</sup>  $n = 21$  male/14 female); Error bars represents mean  $\pm$  SEM. (E) qRT-PCR showing reduction of mRNA expression of *Cul3* in adult cerebral cortex of *Cul3*<sup>+/-</sup> mice (\*\*\* $p < 0.001$ ; two tailed T-test;  $n = 5$  for both genotypes); Error bars represents mean  $\pm$  SEM. (F) Western blot of *Cul3* protein, showing its significant reduction in *Cul3*<sup>+/-</sup> mutant mice cortex ( $p < 0.01$ ;  $n = 6$  for each genotype); hippocampus ( $p < 0.001$ ;  $n = 6$  for each genotype) and cerebellum ( $p < 0.001$ ;  $n = 6$  for each genotype); Error bars represents mean  $\pm$  SD. Two tailed T-test was used for calculating statistical significance for D-F. Dots represents independent mice.

**Figure 2. *Cul3*<sup>+/-</sup> mice have altered brain morphology.** (A) Voxel-wise analysis highlighting significant differences in relative volumes throughout the brain between WT and *Cul3*<sup>+/-</sup> mice with 5% false discovery rate (FDR). Scale bar 2.7-10.7 indicates decreasing FDR, where 2.7=5% FDR. Red color signifies increased and blue color signifies decreased brain volume compared with WT brain. (B) *Cul3*<sup>+/-</sup> mice have reduced absolute brain volume (\*\* $p < 0.01$ ) compared to WT mice (WT  $n = 18$ , *Cul3*<sup>+/-</sup>  $n = 20$ ). (C) Reduced relative gray matter volume in *Cul3*<sup>+/-</sup> mouse brain (\* $p < 0.05$ ). (D) No significance difference is observed in relative white matter volume. (E) MRI revealed significant reduction in relative volume, normalized by absolute volume, of primary somatosensory cortex (\* $p < 0.05$ ); entorhinal cortex (\*\*\* $p < 0.001$ ); cerebellum (\*\* $p < 0.01$ ). (F) Increase in relative volume of midbrain (\*\*\* $p < 0.001$ ); hypothalamus (\*\*\* $p < 0.001$ ); thalamus (\*\*\* $p < 0.001$ ; WT  $n = 18$ , *Cul3*<sup>+/-</sup>  $n = 20$ ). (G) Reduced cortical thickness is observed by MRI in *Cul3*<sup>+/-</sup> mice. (H) Reduced cortical thickness of somatosensory cortex in *Cul3*<sup>+/-</sup> mice, left panel shows somatosensory cortex region stained with NeuN (mature neuron marker) and BRN2 (layer II-IV marker); reduction of total cortical thickness and density of NeuN and BRN2 positive cells/area in layer II-IV are observed (\* $p < 0.05$ ; two tailed T-test,  $n = 6$  for each genotype). (I) Increased apoptosis in *Cul3*<sup>+/-</sup> mice as measured by TUNEL assay on 14DIV primary cortical neurons, the dual positive neurons for PI and BrdU-488 were counted by flow cytometry; (Q4) were considered as apoptotic cells containing BrdU-488/PI+ cells (\*\*\* $p < 0.001$ ;  $n = 9$  for each genotype). Dots represent independent samples; Two tailed T-test used for B-I; error bars represent mean  $\pm$  SD.

**Figure 3. *Cul3*<sup>+/-</sup> mice display hyperactivity, cognitive and social impairments.** (A) *Cul3*<sup>+/-</sup> mice travel longer distances in open field ( $n = 27$  WT;  $n = 29$  *Cul3*<sup>+/-</sup> (\* $p < 0.05$ )) compared with WT mice. (B) The travelling speed (cm/sec) is significantly increased in *Cul3*<sup>+/-</sup> mice (\* $p < 0.05$ ); representative traces of 30 min in open field show *Cul3*<sup>+/-</sup> mice traveling longer distances compared to WT mice. (C) Time bins showing that *Cul3*<sup>+/-</sup> mice travel significantly longer distance in the last 20 min (\* $p < 0.05$ ; \*\* $p < 0.01$ ). (D) No difference in time spent self-grooming between WT and *Cul3*<sup>+/-</sup> mice (WT  $n = 15$ ; *Cul3*<sup>+/-</sup>  $n = 19$ ). (E) *Cul3*<sup>+/-</sup> mice demonstrate significantly reduced



preference for novel object in novel object recognition test (\* $p < 0.05$ ; Two tailed T-test, WT  $n = 18$ ; *Cul3*<sup>+/-</sup>  $n = 20$ ). **(F)** (Upper panel) Schematic diagram of three chamber social interaction test; reduced sniffing time is observed for *Cul3*<sup>+/-</sup> mice while interacting with a novel mouse (vs novel object) as compared to WT mice (WT  $n = 17$ ; *Cul3*<sup>+/-</sup>  $n = 19$ ; \* $p < 0.05$ ; One way ANOVA). **(G)** Reduced sniffing time is observed for *Cul3*<sup>+/-</sup> mice while interacting with a novel mouse (vs familiar mouse) as compared to WT mice (WT  $n = 17$ ; *Cul3*<sup>+/-</sup>  $n = 19$ ) \*\*\* $p < 0.01$ ; One way ANOVA. Dots represent independent animals; error bars represent mean  $\pm$  SD.

**Figure 4. Spatiotemporal differential gene expression analyses identifies dysregulation of cytoskeletal processes by *Cul3* mutation.** **(A)** Heatmap of Gene Ontology terms. Fisher p-value combination analysis was applied to identify 21 clusters of differentially expressed genes impacted by *Cul3* mutation across developmental periods and brain regions. Biological processes impacting more than one cluster are shown. **(B)** Heatmap of genes associated with GO terms from panel (A). Genes from Integrin binding and Cilium-related GO terms are differentially expressed in embryonic period, genes from cell adhesion and migration GO terms are differentially expressed in early postnatal period, and genes from cytoskeleton-related GO terms are differentially expressed in adult period. **(C)** Enrichment of differentially expressed genes from each period with literature-curated gene lists with previous evidence for involvement in autism. These lists include pre- and post-synaptic genes from SynaptomeDB; syndromic and highly ranked (1 and 2) genes from SFARI Gene database (<https://gene.sfari.org/database/gene-scoring/>); genes with probability of loss-of-function intolerance (pLI) > 0.99 as reported by the Exome Aggregation Consortium; constrained genes; and FMRP target genes. Number of overlapped genes (in parenthesis) and odds ratio are indicated inside each cell, and provided only for FDR < 0.05 and OR > 1. **(D)** Enrichment of differentially expressed genes from each brain region with literature-curated gene lists with previous evidence for involvement in autism. See description of lists above.

**Figure 5. Differential protein expression and weighted protein co-expression network analyses of *Cul3*<sup>+/-</sup> mice.** **(A)** (Left panel) Volcano plots of differentially expressed proteins between *Cul3*<sup>+/-</sup> and WT embryonic cortex identified from quantitative TMT-MS proteomic profiling. *Cul3* is colored in pink. Proteins colored in red are upregulated and proteins colored in blue are downregulated in *Cul3*<sup>+/-</sup> embryonic cortex. (Middle panel) Gene Ontology enrichment of up- and downregulated proteins are shown as bar plots. Contribution of up- or down-regulated proteins to specific GO terms are shown in blue and red, respectively. (Right panel) Expression Heatmap of proteins associated with neuron projection development in WT and *Cul3*<sup>+/-</sup> embryonic cortex. **(B)** (Left panel) Venn diagram representing shared DEPs among three developmental periods (FDR  $\leq 0.15$ ). 64 proteins are shared among all periods for both cortex and cerebellum. (Right panel) Expression Heatmap of three shared DEPs (INA, Pls3 and VIM) in all periods and regions shows upregulation in *Cul3*<sup>+/-</sup> mutant vs WT. **(C)** (Upper panel) Western blot of Pls3 in embryonic cortex. (Bottom panel) Densitometry analysis of Western Blot is shown below. Data is represented as mean  $\pm$  SEM ( $n = 3$  per genotype; \*\* $p < 0.01$ ; Two tailed t-Test). Significance above bars represents comparison against WT. **(D-E)** Enrichment of differentially expressed proteins combined by period **(D)** and region **(E)** with literature-curated gene lists with previous evidence for involvement in autism. Number of overlapped proteins (in parenthesis) and odds ratio are shown inside each cell, and provided only for FDR < 0.05 and OR > 1. **(F)** Hierarchical clustering of protein co-expression modules by module eigengene for *Cul3*<sup>+/-</sup> cortex. Module-genotype associations (\* FDR < 0.1) are shown below each module. A total of 9, 5, 7 modules were significantly associated with *Cul3*<sup>+/-</sup> genotype in embryonic, early postnatal and adult cortex respectively. Module enrichment analyses against literature-curated gene lists with previous evidence for involvement in autism are shown at the bottom (\* FDR < 0.05).



**Figure 6. Altered neuron growth and network activity in *Cul3*<sup>+/-</sup> mice. (A-C)** Module-genotype association, module eigengene and GO functional annotations for *blue* neuronal module identified by protein co-expression analyses of embryonic cortex. Dots represent independent animals (n=4 per genotype). **(D)** Module preservation scores of *blue* neuronal module from embryonic cortex as the reference vs. other developmental periods and regions. Modules with Z-summary scores above 2 are preserved. **(E)** Expression Heatmap of proteins from *blue* neuronal module. **(F)** Representative images of 14DIV primary cortical neurons from WT and *Cul3*<sup>+/-</sup> mice, immunostained with MAP2. **(G-I)** Quantification of total dendrite length, neurite number and soma size are shown. Symbols represent independent neurons and color represents littermates. Data is shown as mean ± SD (n=6 per genotype, at least 6-8 neurons per mouse). Significance is calculated using two tailed T-test; \*\*\*p<0.001; \*\*p<0.01. **(J)** Representative raster plots of spontaneous spike activity from 8DIV primary cortical neurons. **(K)** Spontaneous spike activity significantly reduced in *Cul3*<sup>+/-</sup> cortical neurons; \*\*p<0.01, two tailed T-Test. **(L)** Average burst frequency is significantly reduced in *Cul3*<sup>+/-</sup> neurons; \*\*p<0.01; two tailed T-test. n=6-7 mice per genotype; 1.5X10<sup>6</sup> neurons were seeded from each mouse in each MEA plate well, each containing 64 electrodes. Each dot represents independent mouse and color represents littermates.

**Figure 7. Actin cytoskeleton defects are observed in *Cul3*<sup>+/-</sup> mice. (A-C)** Module-genotype association, module eigengene and GO functional annotations for *black* actin module identified by protein co-expression analyses of adult cortex. Dots represent independent animals (n=4 per genotype). **(D)** Representative images of 21DIV primary cortical neurons from WT and *Cul3*<sup>+/-</sup> mice, immunostained with MAP2 (green) and phalloidin-rhodamine (red); stippled boxes show enlarged dendritic segment with F-actin puncta for better visualization. **(E-F)** Quantification of F-actin puncta and F-actin intensity on MAP2 positive dendrites, normalized by dendrite length. Symbols represent independent neurons and color represents littermates. Data is presented as mean ± SD (n=4 per genotype, at least 7-10 neurons per mouse). Significance is calculated using two tailed T-test; \*\*\*p<0.001.

**Figure 8. *Cul3* haploinsufficiency leads to RhoA upregulation and RhoA inhibition rescues dendritic growth deficits. (A)** Representative images of Western Blot analysis of Cul3, total RhoA, and GAPDH loading control in embryonic and adult cortices. Densitometry analysis of Western Blot is shown at the bottom. Data is represented as mean ± SEM (n=6 per genotype). **(B)** Representative images of Western Blot analysis of active RhoA (RhoA-GTP), total RhoA and GAPDH loading control in embryonic cortex. Densitometry analysis of Western Blot is shown at the bottom. Data is represented as mean ± SEM (n=4 per genotype for total RhoA, n=4 per genotype for active RhoA). Significance is calculated using two tailed T-test; \*\*p<0.01. Significance above bars represents comparison against WT. **(C)** Representative images of 14DIV primary cortical neurons. The vehicle (Vh) and Rhosin (Rh) treated cells were immunostained with Map2 and dendrite tracing was performed. **(D)** Rhosin treatment rescues decreased dendrite length phenotype in *Cul3*<sup>+/-</sup> neurons. Symbols represent independent neurons and color represents littermates. Data is presented as mean ± SD (n=2 per genotype, at least 8-10 neurons per mouse). Significance is calculated using One way ANOVA; \*p<0.05.

## Supplementary Figures titles and legends

**Figure S1. Altered brain morphology of *Cul3*<sup>+/-</sup> postnatal day 7 (P7) mice. (A)** Voxel-wise analysis highlighting significant differences in relative volumes throughout the brain between WT and *Cul3*<sup>+/-</sup> mice with 5% false discovery rate (FDR). Scale bar 2-4.9 indicates decreasing FDR, where 2 corresponds to 5% FDR and positive or negative change compared with WT brain. **(B)** *Cul3*<sup>+/-</sup> mice have reduced absolute brain volume (\*\*\*p<0.001) compared with WT mice (n=22 WT, 19 *Cul3*<sup>+/-</sup>). **(C)** MRI revealed significant increase in hypothalamus volume (\*\*\*p<0.001). (D-

F) MRI revealed significant reduction in relative volume (normalized by % total brain volume) of cerebellum (\* $p < 0.05$ ), parieto-temporal cortex (\* $p < 0.05$ ), and frontal cortex (\* $p < 0.05$ ); Dots represent individual samples; Two tailed T-test used for **B-F**; error bars represent mean  $\pm$  SD.

**Figure S2. *Cul3*<sup>+/-</sup> mice do not display anxiety.** (A) *Cul3*<sup>+/-</sup> mice display no preference for the center vs periphery in open field test. (B) 10 min time-bins showing no difference in % time spent in the center in any 10 min intervals. Dots represent independent animals; Two tailed T-test used for **A-B**; error bars represent mean  $\pm$  SD.

**Figure S3. Analysis of developmental milestones and early postnatal behaviors in *Cul3*<sup>+/-</sup> mice.** (A) The timeline used for the early postnatal behavioral assays. (B) The righting reflex is motor ability for a mouse pup to be able to flip onto its feet from a supine position, *Cul3*<sup>+/-</sup> mice display delayed righting reflex as compared to WT mice (n=17 WT, n=19 *Cul3*<sup>+/-</sup>,  $p < 0.01$ ). (C) *Cul3*<sup>+/-</sup> mice display significant vestibular imbalance. The pup's eyes are still closed so fear is not the driving factor to turn away from the cliff's edge (n=15 WT, n=20 *Cul3*<sup>+/-</sup>,  $p < 0.05$ ). (D-K) Both *Cul3*<sup>+/-</sup> and WT mice have no difference in other postnatal behaviors tasks. Dots represent independent animals; Two tailed T-test used for **B-K**; error bars represent mean  $\pm$  SD.

**Figure S4. RNA-seq experimental design and data analysis workflow.** A total of 108 transcriptomes have been sequenced in this study. A rigorous quality control including principal component analyses, upper quartile normalization, removal of unwanted variables (RUV) was used for batch correction.

**Figure S5. Quality control metrics for RNA-seq data.** (A) Sequencing metrics from STAR (2.5.3a) for samples from three periods (embryonic E17.5, early postnatal P7 and adult). (B) Sequencing metrics from PICARD (v2.12) from three periods. (C) Relative log expression values are shown before (left panel) and after (right panel) batch correction using RUVseq for the embryonic cortex samples as an example. (D) First two principal components (PCs) of gene expression values calculated using "prcomp" function in R, are shown before (left panel) and after (right panel) batch correction using RUVseq for the embryonic cortex samples as an example.

**Figure S6. Differentially expressed genes shared across periods and regions.** (A) Venn diagram showing 78 common DEGs across the developmental periods. (B) Venn diagram showing 69 common DEGs across brain regions.

**Figure S7. Differential gene expression for individual periods and regions.** (Left) Volcano plots of differentially expressed genes in *Cul3*<sup>+/-</sup> vs WT for embryonic, early postnatal and adult cortex, hippocampus and cerebellum. Genes colored in red are upregulated in *Cul3*<sup>+/-</sup> compared to WT; genes colored in blue are downregulated in *Cul3*<sup>+/-</sup> compared to WT. (Right) GO-terms enrichment of differentially expressed genes by periods and regions.

**Figure S8. TMT quantitative proteomics experimental design and data analysis workflow.** A total of 48 proteomes (24 each for Cortex and Cerebellum) have been processed in this study by TMT 10-plex labeling followed by LC-MS/MS. Protein Quantification was carried out by Census. Quality control including principal component analyses, ComBat has been performed. LIMMA was implemented for differential protein expression analyses.

**Figure S9. Differential protein expression analyses for individual periods and regions.** (A-E) Volcano plots of differentially expressed proteins in *Cul3*<sup>+/-</sup> vs WT (left column) for early postnatal and adult cortex, and embryonic, early postnatal and adult cerebellum. Proteins colored in red are upregulated in *Cul3*<sup>+/-</sup> compared to WT; proteins colored in blue are downregulated in

*Cul3*<sup>-/-</sup> compared to WT. (Right) GO-terms enrichment of differentially expressed proteins by regions. Early postnatal and adult cerebellum have no GO-term enrichment. **(F)** Venn diagram showing 716 common DEPs across brain regions.

**Figure S10. Protein co-expression modules in *Cul3*<sup>-/-</sup> cerebellum.** Hierarchical clustering of protein co-expression modules by module eigengene for *Cul3*<sup>-/-</sup> cerebellum. Module-genotype associations (\*FDR<0.1) are shown below each module. A total of 8, 1, and 2 modules were significantly associated with *Cul3*<sup>-/-</sup> genotype in embryonic, early postnatal and adult cerebellum, respectively. Module enrichment analyses against literature-curated gene lists with previous evidence for involvement in autism are shown at the bottom (\* FDR<0.05).

## Supplementary Tables titles

**Table S1.** *Cul3* mutational spectrum.

**Table S2.** Brain MRI of *Cul3*<sup>-/-</sup> adult and early postnatal mouse brain.

**Table S3.** Differentially expressed genes (DEGs) in embryonic, early postnatal and adult cortex, hippocampus and cerebellum.

**Table S4.** Gene Ontology enrichment analysis of differentially expressed genes.

**Table S5.** Differentially expressed genes (DEGs) clusters.

**Table S6.** Gene Ontology enrichment analysis of DEG clusters.

**Table S7.** Differentially expressed proteins (DEPs) in embryonic, early postnatal and adult cortex and cerebellum.

**Table S8.** Gene Ontology enrichment analysis of differentially expressed proteins.

**Table S9.** Module membership from protein co-expression (WPCNA) analysis in embryonic, early postnatal and adult cortex and cerebellum.

**Table S10.** Gene Ontology enrichment analysis of protein co-expression modules from WPCNA of cortex.

**Table S11.** Gene Ontology enrichment analysis of protein co-expression modules from WPCNA of cerebellum.

**Table S12.** RNA-seq parameters and quality control metrics from Cutadapt, STAR, Picard, and RNA-SeQC for embryonic E17.5, early postnatal P7, and adult brain representing 108 transcriptomes.

## References

- Azzarelli, R., Kerloch, T., and Pacary, E. (2014). Regulation of cerebral cortex development by Rho GTPases: insights from in vivo studies. *Front Cell Neurosci* 8, 445.
- Chen, Y., Yang, Z., Meng, M., Zhao, Y., Dong, N., Yan, H., Liu, L., Ding, M., Peng, H.B., and Shao, F. (2009). Cullin mediates degradation of RhoA through evolutionarily conserved BTB adaptors to control actin cytoskeleton structure and cell movement. *Mol Cell* 35, 841-855.
- Darnell, J.C., Van Driesche, S.J., Zhang, C., Hung, K.Y., Mele, A., Fraser, C.E., Stone, E.F., Chen, C., Fak, J.J., Chi, S.W., *et al.* (2011). FMRP stalls ribosomal translocation on mRNAs linked to synaptic function and autism. *Cell* 146, 247-261.

- Dong, Z., Chen, W., Chen, C., Wang, H., Cui, W., Tan, Z., Robinson, H., Gao, N., Luo, B., Zhang, L., *et al.* (2019). CUL3 Deficiency Causes Social Deficits and Anxiety-like Behaviors by Impairing Excitation-Inhibition Balance through the Promotion of Cap-Dependent Translation. *Neuron*.
- Dorr, A.E., Lerch, J.P., Spring, S., Kabani, N., and Henkelman, R.M. (2008). High resolution three-dimensional brain atlas using an average magnetic resonance image of 40 adult C57Bl/6J mice. *Neuroimage* 42, 60-69.
- Ellegood, J., Anagnostou, E., Babineau, B.A., Crawley, J.N., Lin, L., Genestine, M., DiCicco-Bloom, E., Lai, J.K., Foster, J.A., Penagarikano, O., *et al.* (2015). Clustering autism: using neuroanatomical differences in 26 mouse models to gain insight into the heterogeneity. *Mol Psychiatry* 20, 118-125.
- Escamilla, C.O., Filonova, I., Walker, A.K., Xuan, Z.X., Holehonnur, R., Espinosa, F., Liu, S., Thyme, S.B., Lopez-Garcia, I.A., Mendoza, D.B., *et al.* (2017). Kctd13 deletion reduces synaptic transmission via increased RhoA. *Nature* 551, 227-231.
- Genovese, C.R., Lazar, N.A., and Nichols, T. (2002). Thresholding of statistical maps in functional neuroimaging using the false discovery rate. *Neuroimage* 15, 870-878.
- Govek, E.E., Hatten, M.E., and Van Aelst, L. (2011). The role of Rho GTPase proteins in CNS neuronal migration. *Dev Neurobiol* 71, 528-553.
- He, L., Diedrich, J., Chu, Y.Y., and Yates, J.R., 3rd (2015). Extracting Accurate Precursor Information for Tandem Mass Spectra by RawConverter. *Anal Chem* 87, 11361-11367.
- Hill, J.M., Lim, M.A., and Stone, M.M. (2008). Developmental Milestones in the Newborn Mouse. Gozes I (eds) *Neuropeptide Techniques Neuromethods* 39, Humana Press.
- Johnson, W.E., Li, C., and Rabinovic, A. (2007). Adjusting batch effects in microarray expression data using empirical Bayes methods. *Biostatistics* 8, 118-127.
- Kang, H.J., Kawasawa, Y.I., Cheng, F., Zhu, Y., Xu, X., Li, M., Sousa, A.M., Pletikos, M., Meyer, K.A., Sedmak, G., *et al.* (2011). Spatio-temporal transcriptome of the human brain. *Nature* 478, 483-489.
- Karczewski, K.J., Weisburd, B., Thomas, B., Solomonson, M., Ruderfer, D.M., Kavanagh, D., Hamamsy, T., Lek, M., Samocha, K.E., Cummings, B.B., *et al.* (2017). The ExAC browser: displaying reference data information from over 60 000 exomes. *Nucleic Acids Res* 45, D840-D845.
- Khatri, N., Gilbert, J.P., Huo, Y., Sharaflari, R., Nee, M., Qiao, H., and Man, H.Y. (2018). The Autism Protein Ube3A/E6AP Remodels Neuronal Dendritic Arborization via Caspase-Dependent Microtubule Destabilization. *J Neurosci* 38, 363-378.
- Krey, J.F., Pasca, S.P., Shcheglovitov, A., Yazawa, M., Schwemberger, R., Rasmusson, R., and Dolmetsch, R.E. (2013). Timothy syndrome is associated with activity-dependent dendritic retraction in rodent and human neurons. *Nat Neurosci* 16, 201-209.
- Lin, G.N., Corominas, R., Lemmens, I., Yang, X., Tavernier, J., Hill, D.E., Vidal, M., Sebat, J., and Iakoucheva, L.M. (2015). Spatiotemporal 16p11.2 Protein Network Implicates Cortical Late Mid-Fetal Brain Development and KCTD13-Cul3-RhoA Pathway in Psychiatric Diseases. *Neuron* 85, 742-754.
- Malhotra, D., and Sebat, J. (2012). CNVs: harbingers of a rare variant revolution in psychiatric genetics. *Cell* 148, 1223-1241.
- McAlister, G.C., Nusinow, D.P., Jedrychowski, M.P., Wuhr, M., Huttlin, E.L., Erickson, B.K., Rad, R., Haas, W., and Gygi, S.P. (2014). MultiNotch MS3 enables accurate, sensitive, and multiplexed detection of differential expression across cancer cell line proteomes. *Anal Chem* 86, 7150-7158.
- Moore, S.M., Seidman, J.S., Ellegood, J., Gao, R., Savchenko, A., Troutman, T.D., Abe, Y., Stender, J., Lee, D., Wang, S., *et al.* (2019). Setd5 haploinsufficiency alters neuronal network connectivity and leads to autistic-like behaviors in mice. *Transl Psychiatry* 9, 24.



- Nieman, B.J., Bishop, J., Dazai, J., Bock, N.A., Lerch, J.P., Feintuch, A., Chen, X.J., Sled, J.G., and Henkelman, R.M. (2007). MR technology for biological studies in mice. *NMR Biomed* 20, 291-303.
- Nieman, B.J., van Eede, M.C., Spring, S., Dazai, J., Henkelman, R.M., and Lerch, J.P. (2018). MRI to Assess Neurological Function. *Curr Protoc Mouse Biol* 8, e44.
- O'Roak, B.J., Vives, L., Girirajan, S., Karakoc, E., Krumm, N., Coe, B.P., Levy, R., Ko, A., Lee, C., Smith, J.D., *et al.* (2012). Sporadic autism exomes reveal a highly interconnected protein network of de novo mutations. *Nature* 485, 246-250.
- Park, S.K., Venable, J.D., Xu, T., and Yates, J.R., 3rd (2008). A quantitative analysis software tool for mass spectrometry-based proteomics. *Nat Methods* 5, 319-322.
- Petroski, M.D., and Deshaies, R.J. (2005). Function and regulation of cullin-RING ubiquitin ligases. *Nat Rev Mol Cell Biol* 6, 9-20.
- Phipson, B., Lee, S., Majewski, I.J., Alexander, W.S., and Smyth, G.K. (2016). Robust Hyperparameter Estimation Protects against Hypervariable Genes and Improves Power to Detect Differential Expression. *Ann Appl Stat* 10, 946-963.
- Pirooznia, M., Wang, T., Avramopoulos, D., Valle, D., Thomas, G., Haganir, R.L., Goes, F.S., Potash, J.B., and Zandi, P.P. (2012). SynaptomeDB: an ontology-based knowledgebase for synaptic genes. *Bioinformatics* 28, 897-899.
- Pucilowska, J., Vithayathil, J., Tavares, E.J., Kelly, C., Karlo, J.C., and Landreth, G.E. (2015). The 16p11.2 deletion mouse model of autism exhibits altered cortical progenitor proliferation and brain cytoarchitecture linked to the ERK MAPK pathway. *J Neurosci* 35, 3190-3200.
- Qin, L., Ma, K., Wang, Z.J., Hu, Z., Matas, E., Wei, J., and Yan, Z. (2018). Social deficits in Shank3-deficient mouse models of autism are rescued by histone deacetylase (HDAC) inhibition. *Nat Neurosci* 21, 564-575.
- Rapanelli, M., Tan, T., Wang, W., Wang, X., Wang, Z.J., Zhong, P., Frick, L., Qin, L., Ma, K., Qu, J., and Yan, Z. (2019). Behavioral, circuitry, and molecular aberrations by region-specific deficiency of the high-risk autism gene Cul3. *Mol Psychiatry*.
- Rau, A., Marot, G., and Jaffrezic, F. (2014). Differential meta-analysis of RNA-seq data from multiple studies. *BMC Bioinformatics* 15, 91.
- Reimand, J., Kull, M., Peterson, H., Hansen, J., and Vilo, J. (2007). g:Profiler--a web-based toolset for functional profiling of gene lists from large-scale experiments. *Nucleic Acids Res* 35, W193-200.
- Richter, M., Murtaza, N., Scharrenberg, R., White, S.H., Johanns, O., Walker, S., Yuen, R.K.C., Schwanke, B., Bedurftig, B., Henis, M., *et al.* (2018). Altered TAO2 activity causes autism-related neurodevelopmental and cognitive abnormalities through RhoA signaling. *Mol Psychiatry*.
- Risso, D., Ngai, J., Speed, T.P., and Dudoit, S. (2014). Normalization of RNA-seq data using factor analysis of control genes or samples. *Nat Biotechnol* 32, 896-902.
- Risso, D., Schwartz, K., Sherlock, G., and Dudoit, S. (2011). GC-content normalization for RNA-Seq data. *BMC Bioinformatics* 12, 480.
- Ritchie, M.E., Phipson, B., Wu, D., Hu, Y., Law, C.W., Shi, W., and Smyth, G.K. (2015). limma powers differential expression analyses for RNA-sequencing and microarray studies. *Nucleic Acids Res* 43, e47.
- Robinson, M.D., McCarthy, D.J., and Smyth, G.K. (2010). edgeR: a Bioconductor package for differential expression analysis of digital gene expression data. *Bioinformatics* 26, 139-140.
- Samocha, K.E., Robinson, E.B., Sanders, S.J., Stevens, C., Sabo, A., McGrath, L.M., Kosmicki, J.A., Rehnstrom, K., Mallick, S., Kirby, A., *et al.* (2014). A framework for the interpretation of de novo mutation in human disease. *Nat Genet* 46, 944-950.
- Sanders, S.J., He, X., Willsey, A.J., Ercan-Sencicek, A.G., Samocha, K.E., Cicek, A.E., Murtha, M.T., Bal, V.H., Bishop, S.L., Dong, S., *et al.* (2015). Insights into Autism Spectrum Disorder Genomic Architecture and Biology from 71 Risk Loci. *Neuron* 87, 1215-1233.



- Satterstrom, F.K., Kosmicki, J.A., Wang, J., Breen, M.S., De Rubeis, S., An, J.Y., Peng, M., Collins, R., Grove, J., Klei, L., *et al.* (2020). Large-Scale Exome Sequencing Study Implicates Both Developmental and Functional Changes in the Neurobiology of Autism. *Cell*.
- Shang, X., Marchioni, F., Sipes, N., Evelyn, C.R., Jerabek-Willemsen, M., Duhr, S., Seibel, W., Wortman, M., and Zheng, Y. (2012). Rational design of small molecule inhibitors targeting RhoA subfamily Rho GTPases. *Chem Biol* 19, 699-710.
- Singer, J.D., Gurian-West, M., Clurman, B., and Roberts, J.M. (1999). Cullin-3 targets cyclin E for ubiquitination and controls S phase in mammalian cells. *Genes Dev* 13, 2375-2387.
- Spencer Noakes, T.L., Henkelman, R.M., and Nieman, B.J. (2017). Partitioning k-space for cylindrical three-dimensional rapid acquisition with relaxation enhancement imaging in the mouse brain. *NMR Biomed* 30.
- Steadman, P.E., Ellegood, J., Szulc, K.U., Turnbull, D.H., Joyner, A.L., Henkelman, R.M., and Lerch, J.P. (2014). Genetic effects on cerebellar structure across mouse models of autism using a magnetic resonance imaging atlas. *Autism Res* 7, 124-137.
- Tabb, D.L., McDonald, W.H., and Yates, J.R., 3rd (2002). DTASelect and Contrast: tools for assembling and comparing protein identifications from shotgun proteomics. *J Proteome Res* 1, 21-26.
- Ullmann, J.F., Watson, C., Janke, A.L., Kurniawan, N.D., and Reutens, D.C. (2013). A segmentation protocol and MRI atlas of the C57BL/6J mouse neocortex. *Neuroimage* 78, 196-203.
- Walker, B.A., Ji, S.J., and Jaffrey, S.R. (2012). Intra-axonal translation of RhoA promotes axon growth inhibition by CSPG. *J Neurosci* 32, 14442-14447.
- Xu, T., Park, S.K., Venable, J.D., Wohlschlegel, J.A., Diedrich, J.K., Cociorva, D., Lu, B., Liao, L., Hewel, J., Han, X., *et al.* (2015). ProLuCID: An improved SEQUEST-like algorithm with enhanced sensitivity and specificity. *J Proteomics* 129, 16-24.
- Yi, F., Danko, T., Botelho, S.C., Patzke, C., Pak, C., Wernig, M., and Sudhof, T.C. (2016). Autism-associated SHANK3 haploinsufficiency causes Ih channelopathy in human neurons. *Science* 352, aaf2669.
- Zhang, B., and Horvath, S. (2005). A general framework for weighted gene co-expression network analysis. *Stat Appl Genet Mol Biol* 4, Article17.
- Zhang, H., and Macara, I.G. (2008). The PAR-6 polarity protein regulates dendritic spine morphogenesis through p190 RhoGAP and the Rho GTPase. *Dev Cell* 14, 216-226.

# Figure 1

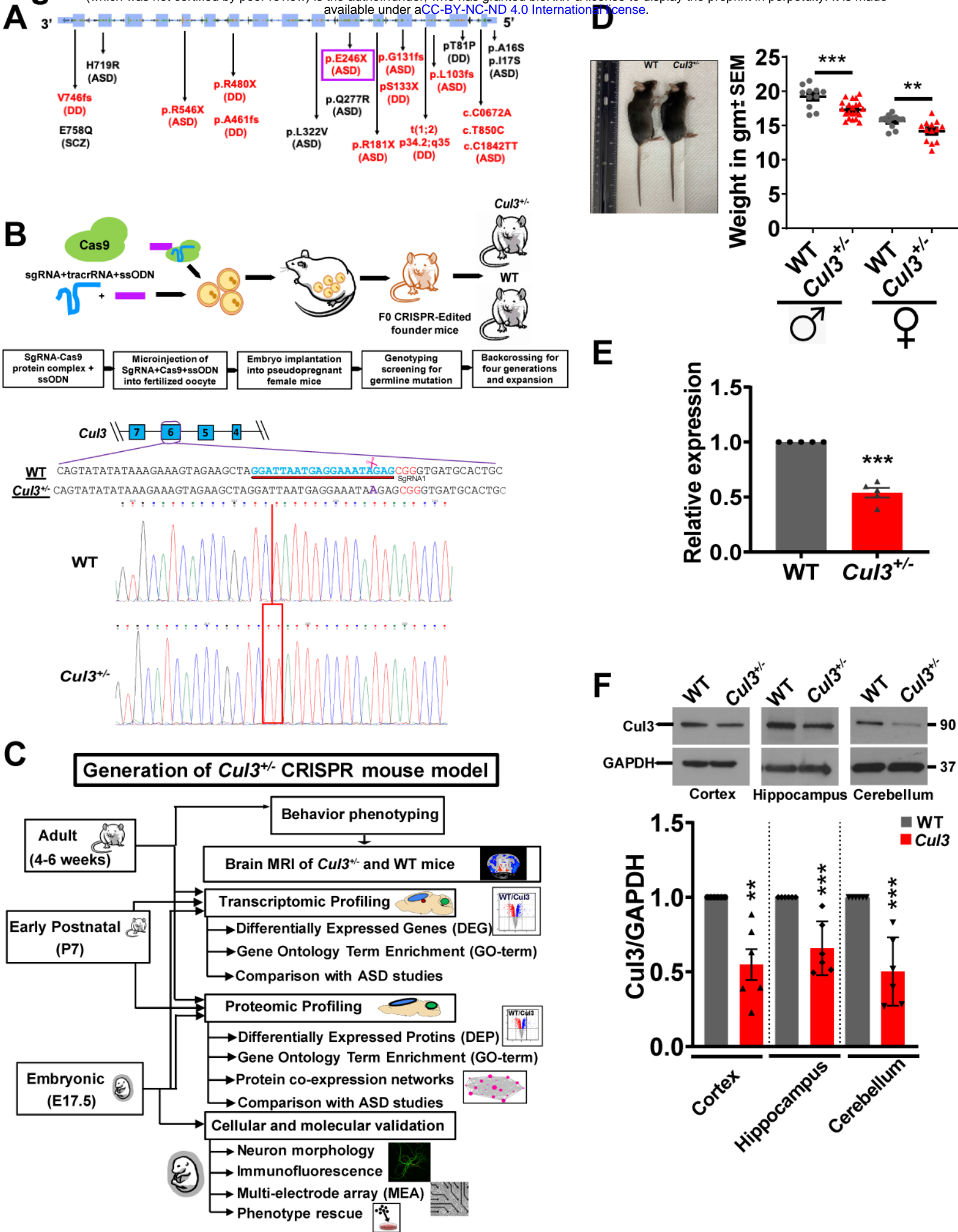
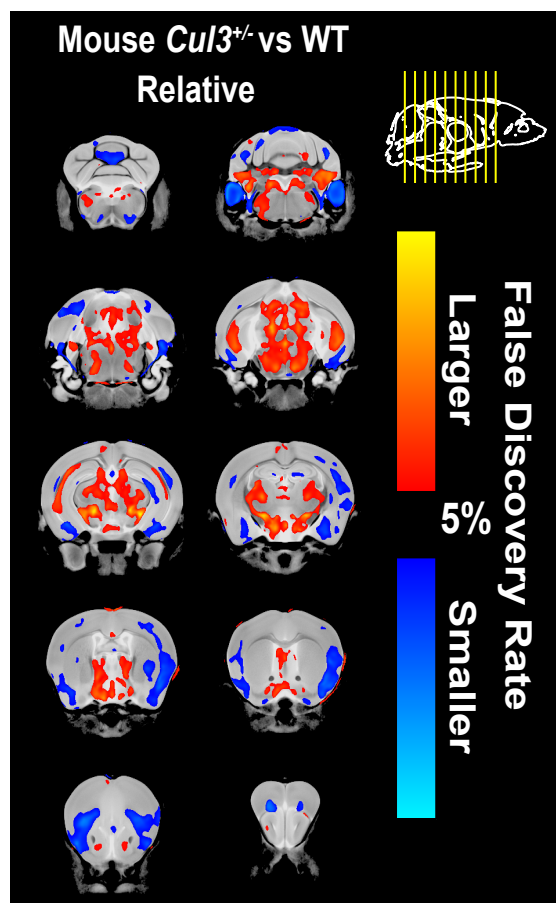
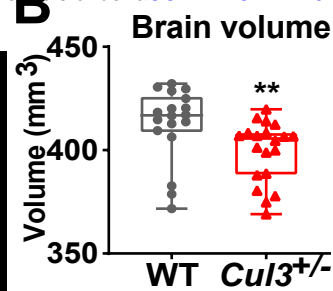


# Figure 2

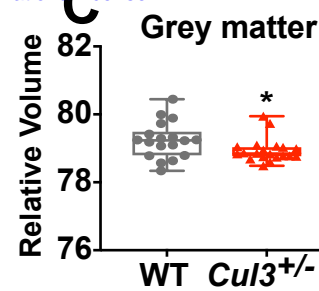
A



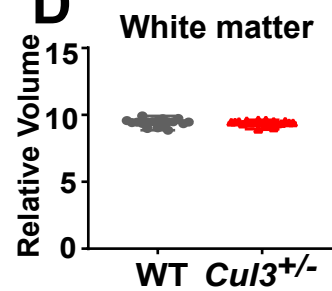
B



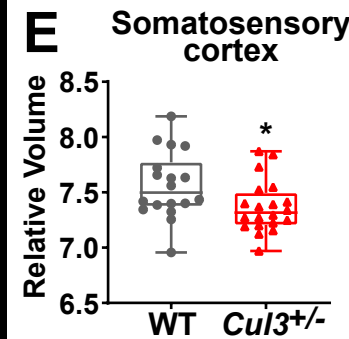
C



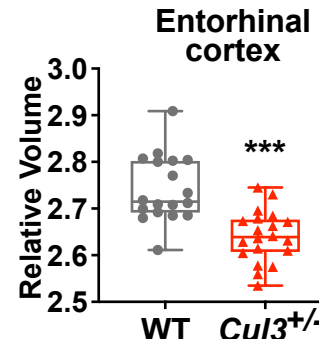
D



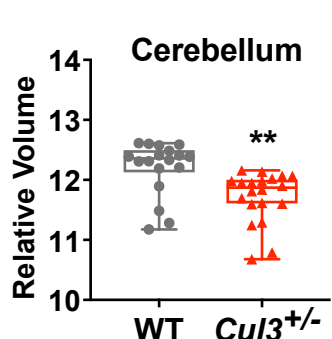
E



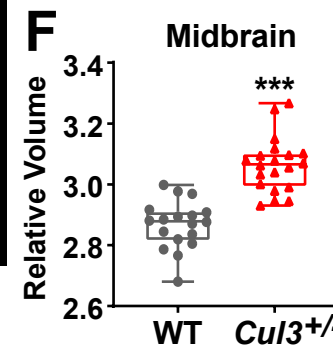
F



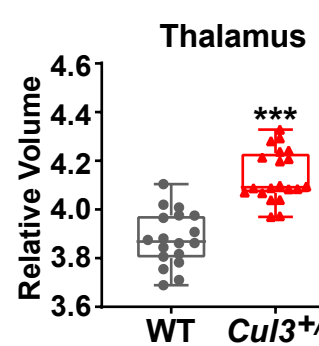
G



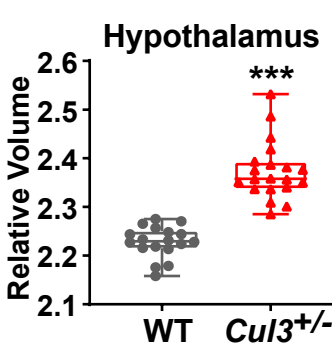
H



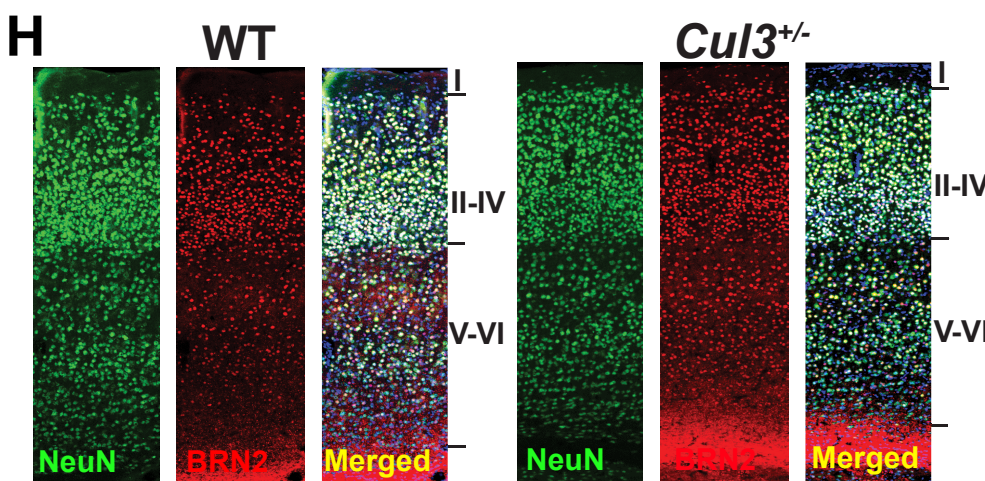
I



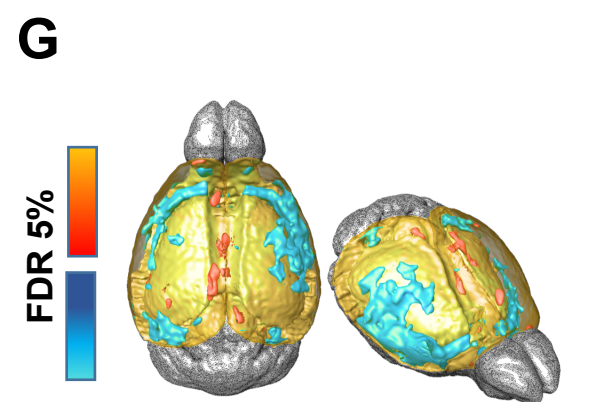
J



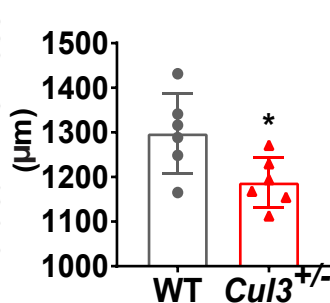
H



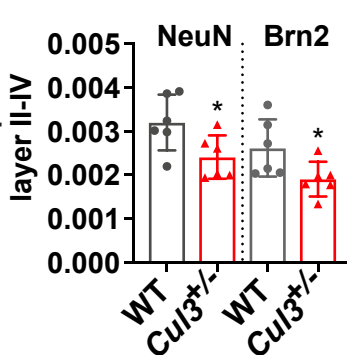
G



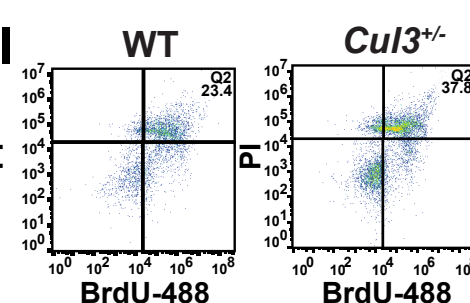
Cortical Thickness (μm)



Cells/μm<sup>2</sup> layer II-IV



PI



Tunel-PI positive cells (relative to WT)

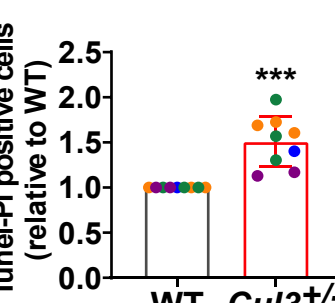


# Figure 3

bioRxiv preprint doi: <https://doi.org/10.1101/2020.02.07.939256>; this version posted February 12, 2020. The copyright holder for this preprint (which was not certified by peer review) is the author/funder, who has granted bioRxiv a license to display the preprint in perpetuity. It is made available under aCC-BY-NC-ND 4.0 International license.

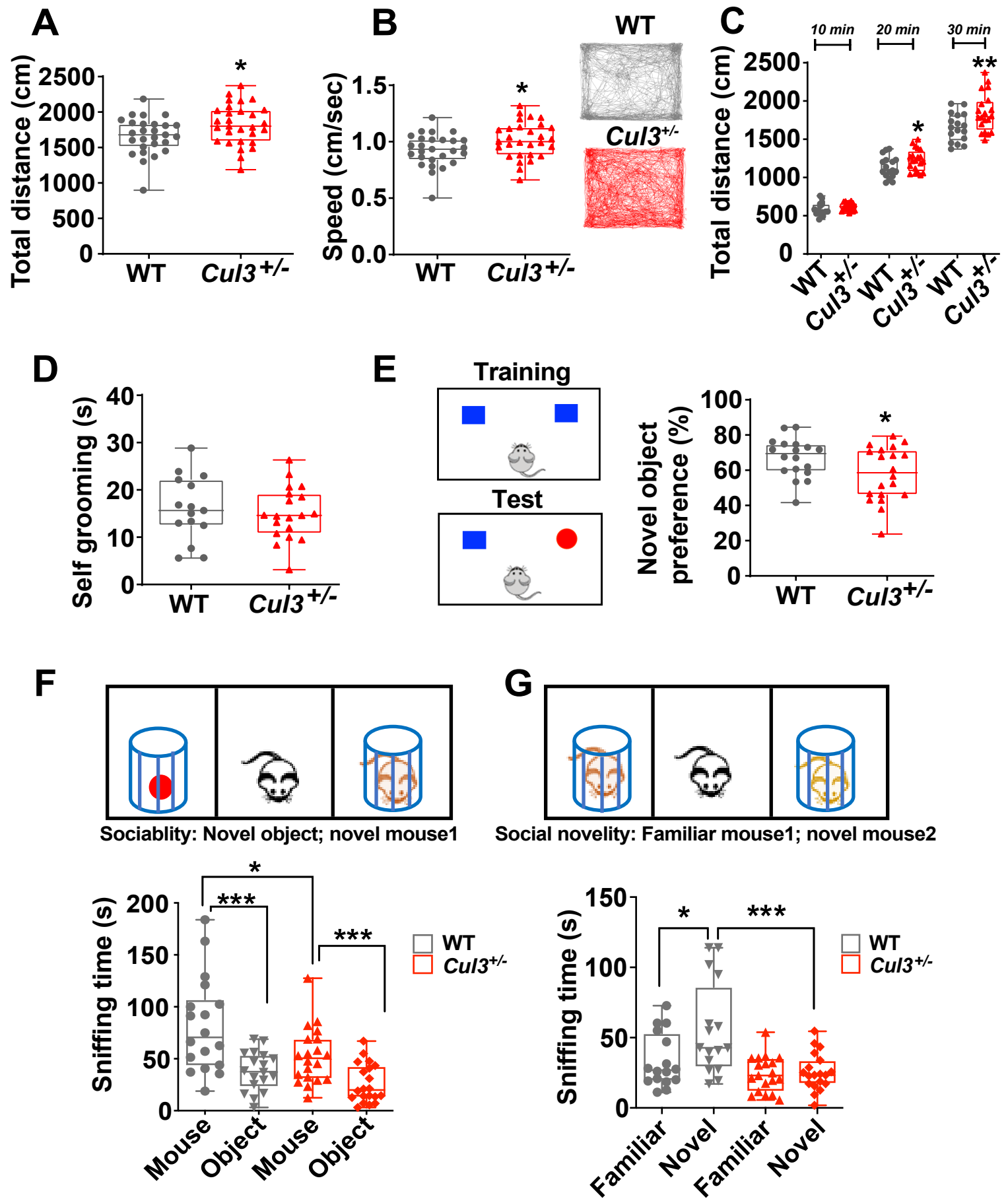
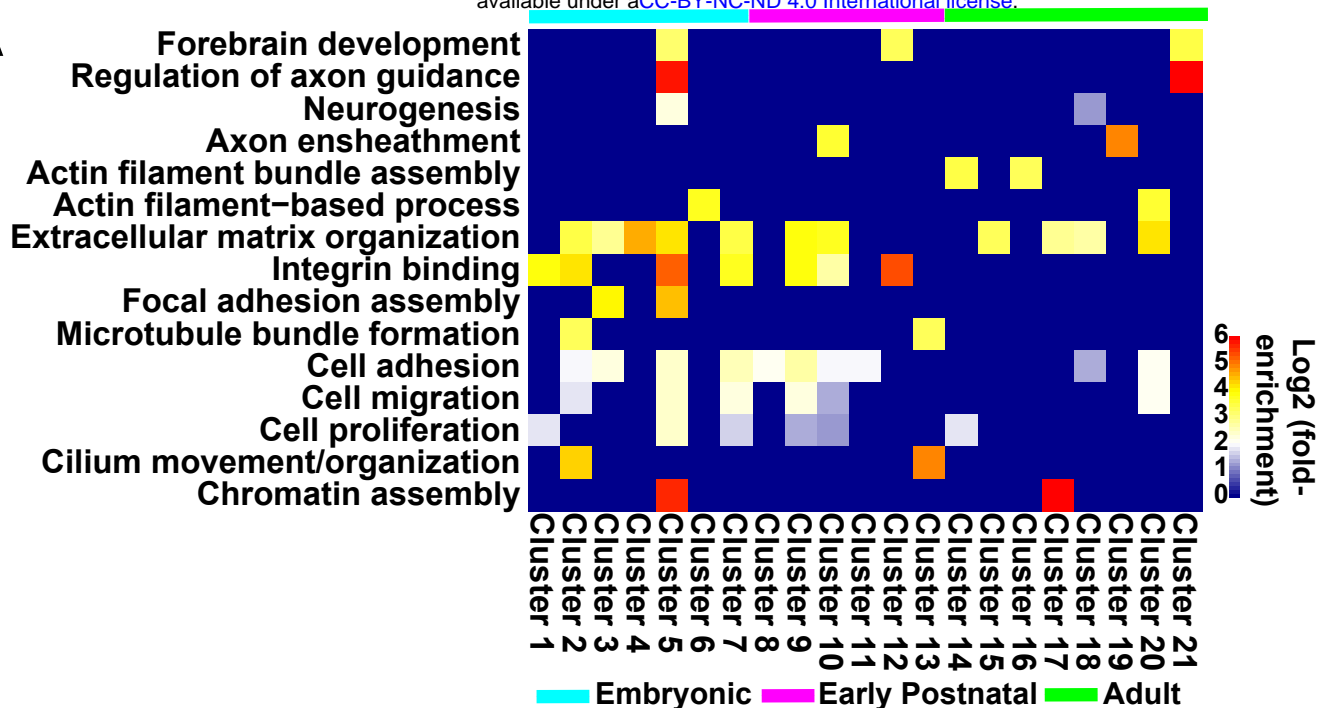


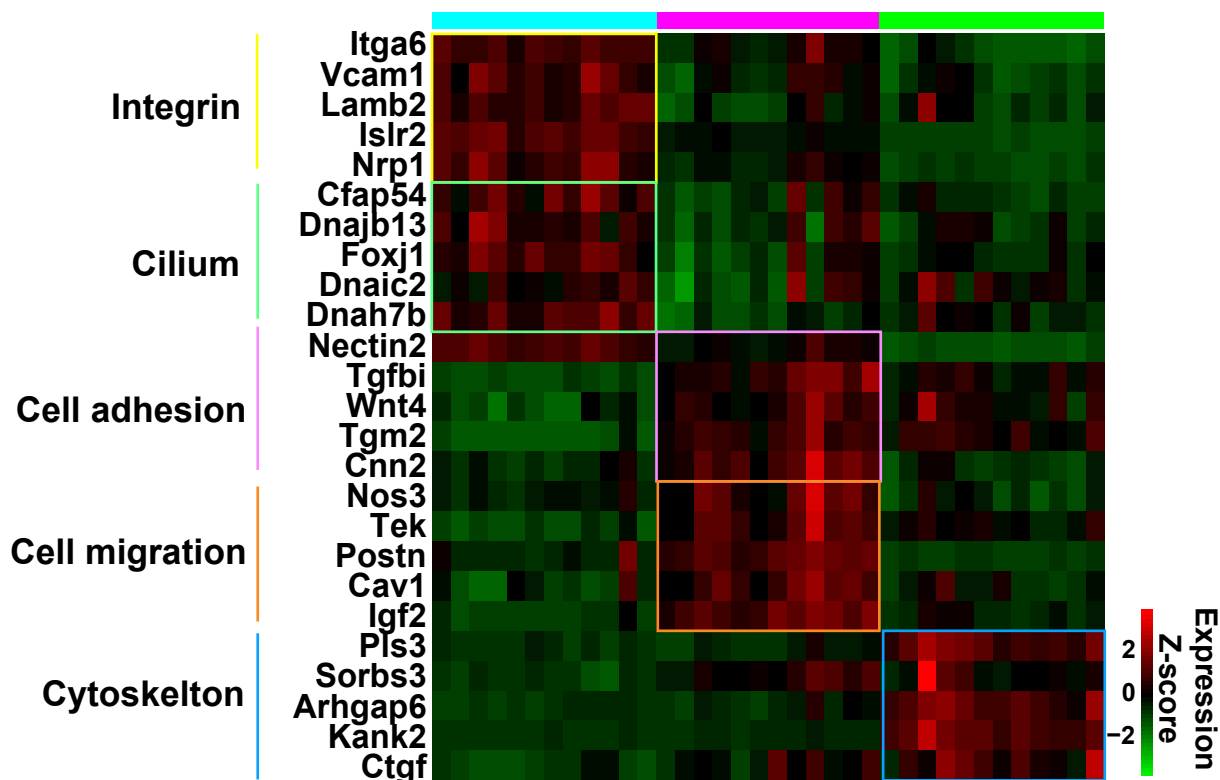


# Figure 4

**A**



**B**



**C**

DEG				DEG			
	Embryonic	Early Postnatal	Adult		CX	HIP	CB
Presynaptic	1.72 (7)	2.39* (16)	2.11* (16)	Presynaptic	1.99* (8)	2.44* (22)	2.66* (15)
Postsynaptic	1.13 (26)	2.04* (75)	2.05* (85)	Postsynaptic	1.62* (36)	2.19* (108)	1.71* (54)
Sfari_S_1_2	2.25 (5)	2.73* (10)	1.9* (8)	Sfari_S_1_2	2.28* (5)	2.42* (12)	2.24* (7)
SatterstromASD	3.32* (4)	3.53* (7)	1.72 (4)	SatterstromASD	5.16* (6)	2.18* (6)	2.33 (4)
pLI0.99	1.55* (36)	1.85* (71)	1.75* (76)	pLI0.99	1.8* (41)	1.88* (97)	1.79* (58)
FMRP targets	0.94 (10)	2.36* (40)	2.3* (44)	FMRP targets	1.25 (13)	2.13* (49)	2.45* (35)

$-\log_{10}$ FDR color scale: 2.5 (blue) to 10.0 (red)

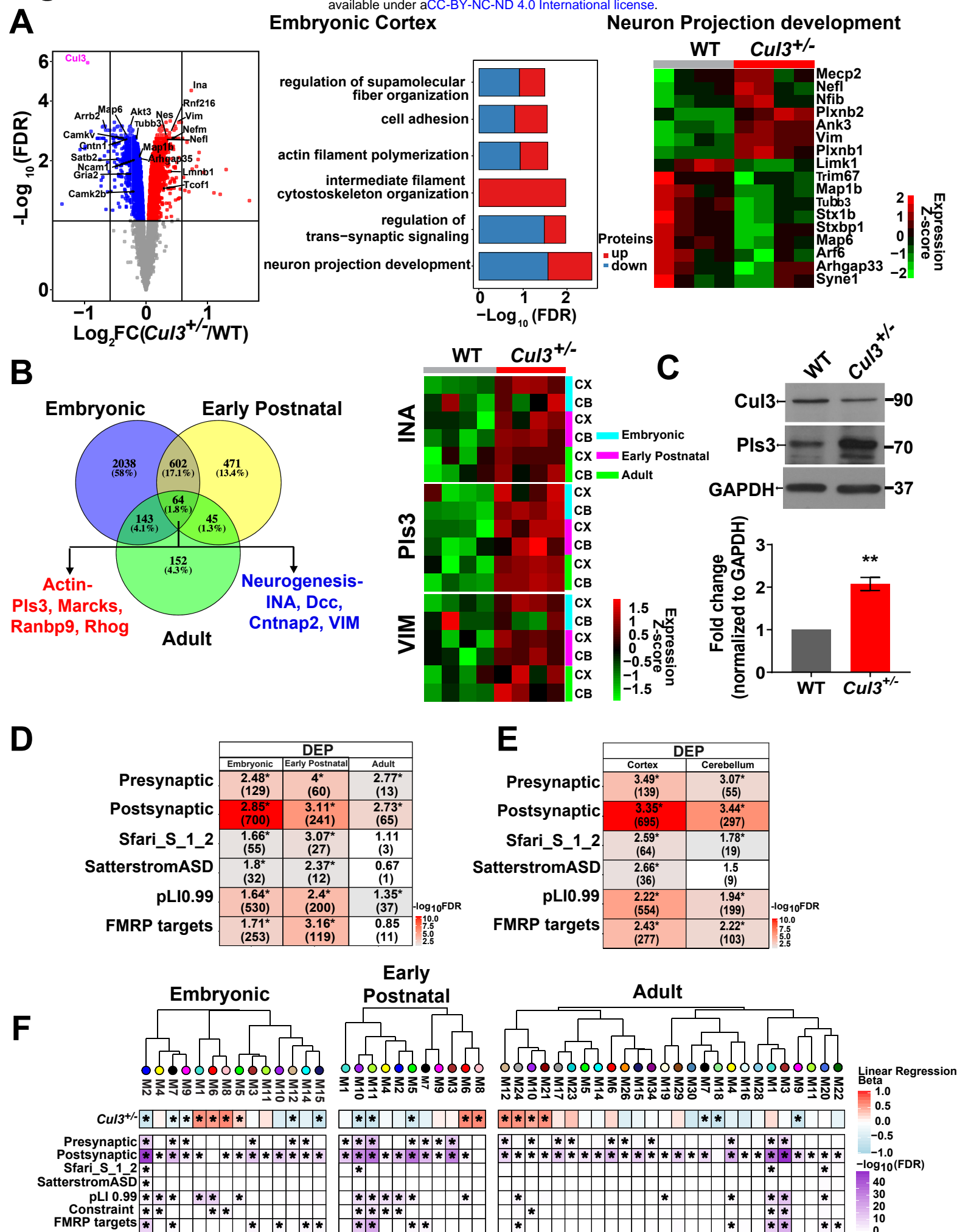


# Figure 6

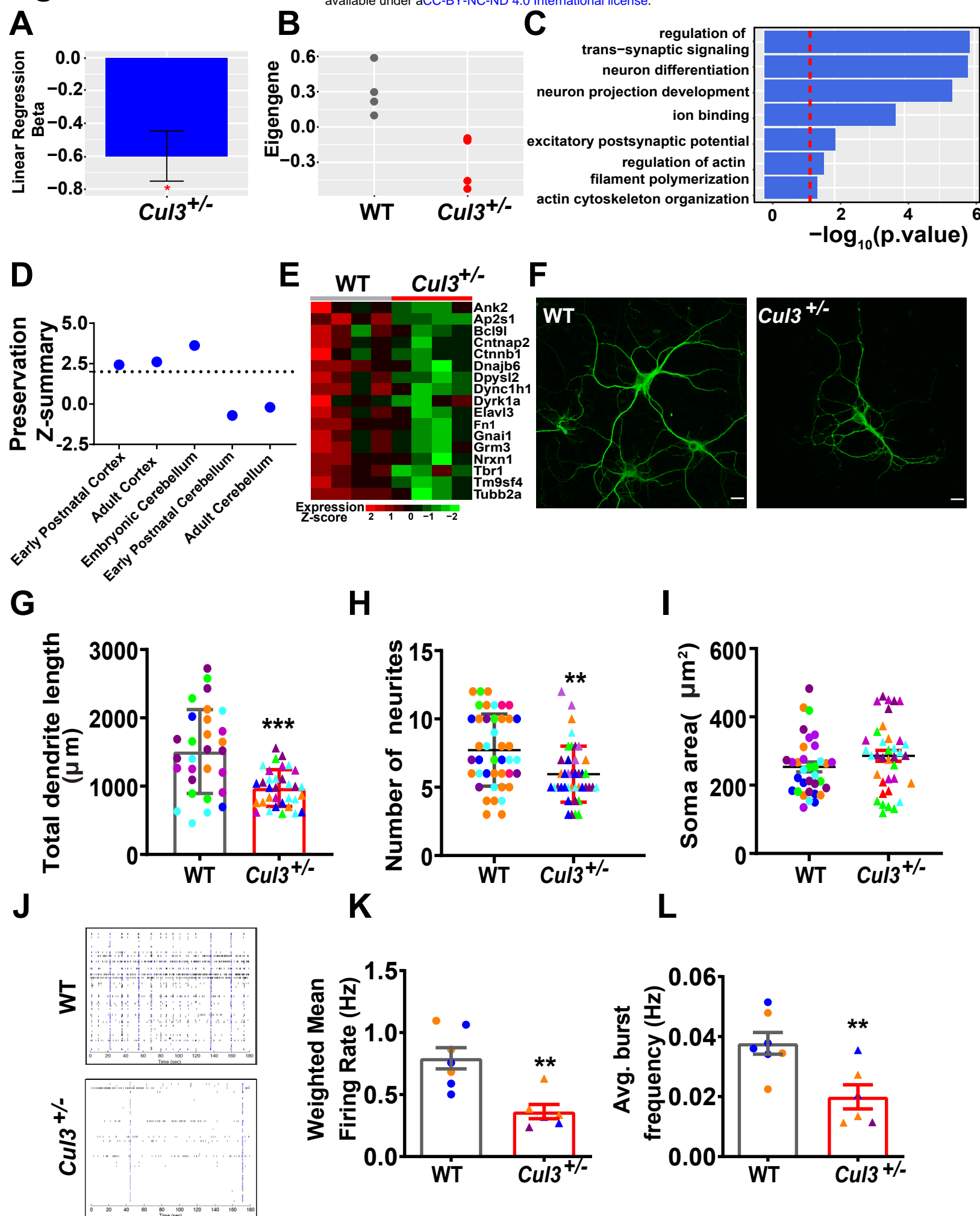


# Figure 7

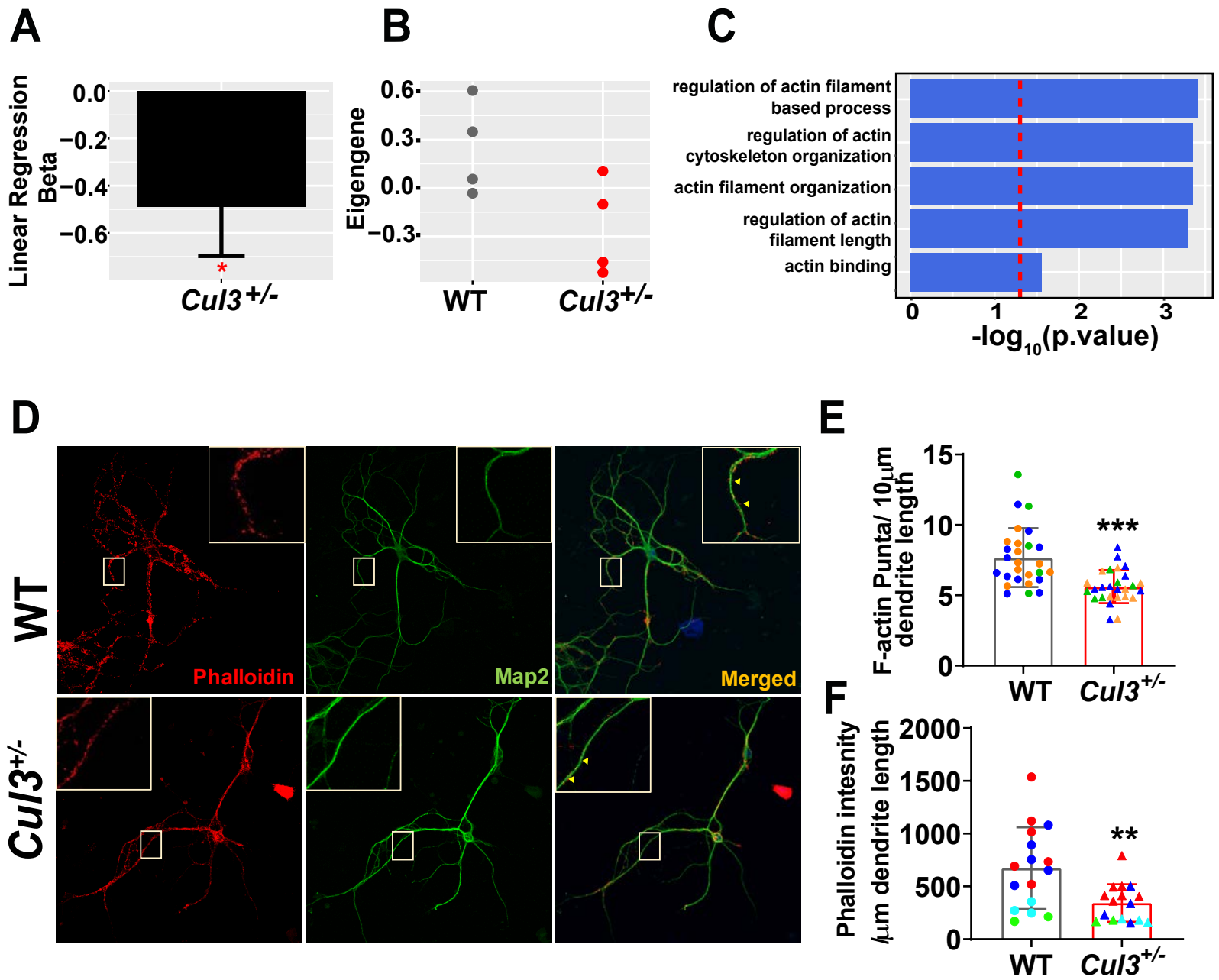
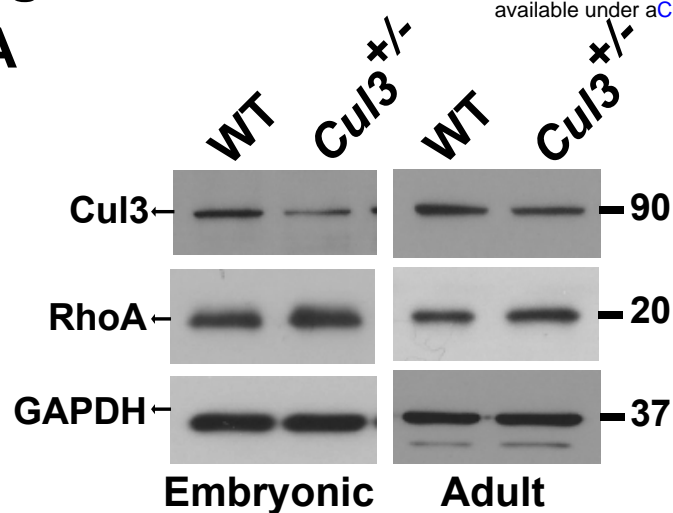


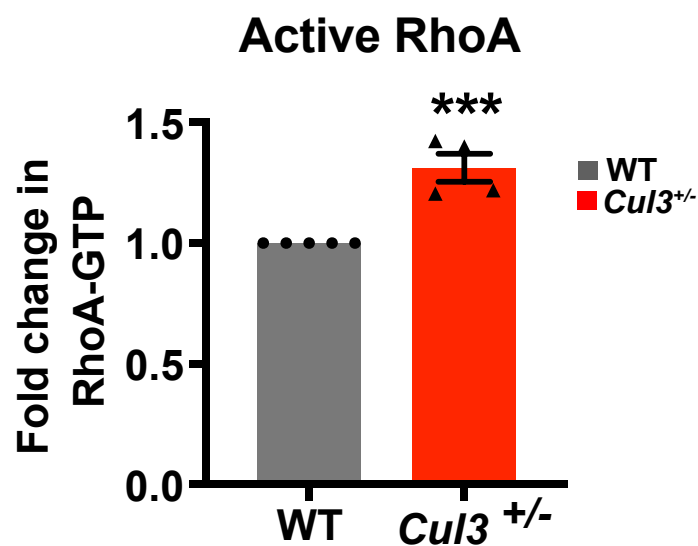
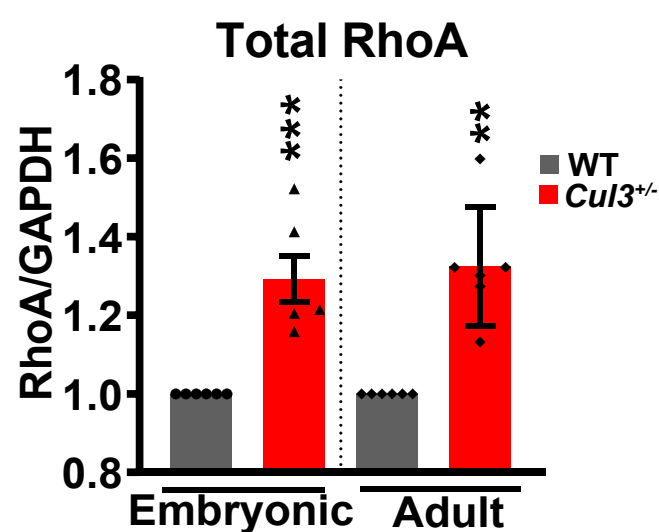
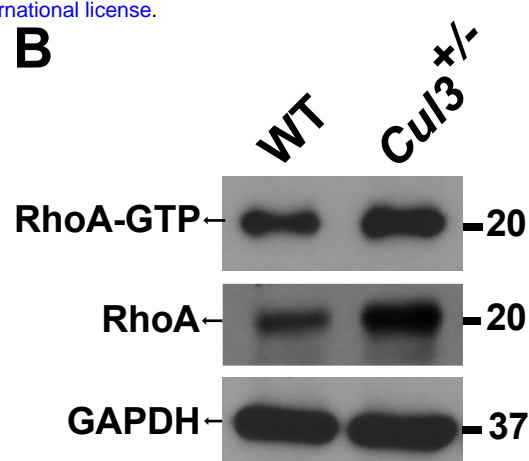


# Figure 8

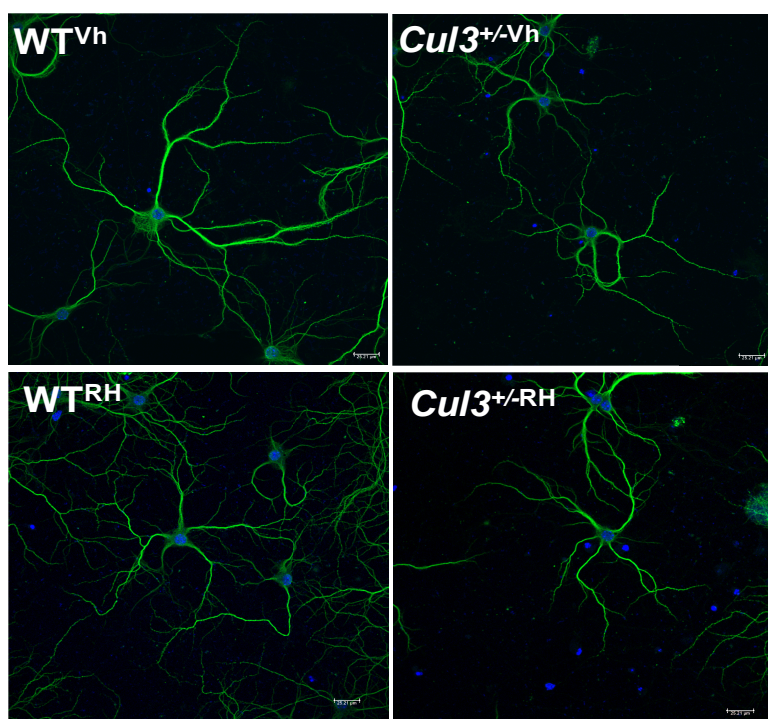
**A**



**B**



**C**



**D**

